A comprehensive experimental study and numerical analysis of coefficient of friction of nanocomposite coatings

Mian Hammad Nazir [a,*], Zulfiqar Ahmad Khan [b], Muhammad Majid Hussain [a], Abdullah Rahil [a], Syed Zohaib Javaid Zaidi [c]

[a] *University of South Wales, Treforest, CF37 1DL, UK*
[b] *NanoCorr, Energy and Modelling Research Group (NCEM), Department of Design and Engineering, Bournemouth University Talbot Campus, Dorset, Poole, BH12 5BB, UK*
[c] *Institute of Chemical Engineering and Technology, University of Punjab, Lahore, Pakistan*

HIGHLIGHTS

- The friction behaviour of nano-composite coatings using oscillating-reciprocating condition has been simulated.
- Pre and Pro-test comparison of Nickel/Graphene and pure-Nickel coatings is conducted using characterisation techniques.
- Four types of tests were performed to compare the COF of Nickel/Graphene and pure-Nickel coatings.
- The post-tests revealed that Ni exhibited higher COF compared to Nickel/Graphene.
- A novel 2-D predictive model integrating the wear concepts with the microstructural and lubrication concepts is developed.

ARTICLE INFO

ABSTRACT

A comprehensive study of nanocomposite coating friction behaviour in oscillating-reciprocating simulations with steel balls is presented. Graphene/Nickel (Ni/GPL) and pure Nickel (Ni) coatings have been studied. SEM, EDS, and AFM analyses of coatings pre-test were performed to characterise the coatings in addition to tests to compare the coefficients of friction 'COF' between pure Ni and Ni/GPL. Based on microscopic characterisation of wear tracks, wear on counter carbon steel balls, and "U-shaped" wear depth profiles of wear tracks, it was determined that Ni had a higher coefficient of friction than Ni/GPL. A novel 2-D predictive numerical model was developed to examine the wear of nanocomposite coatings that integrates the microstructural and lubrication concepts. Predictions from newly developed model and the experimental results are in close agreement. While significant research has been conducted to understand the frictional performance of nanocomposite coatings, a novel and reliable predictive model is still needed for analyzing nanocomposite coatings COF in the context of design. The research will impact the automotive, aerospace, renewable energy, high-end manufacturing, and renewable energy sectors.

1. Introduction

During the past recent years, significant body of research has been performed in development and enhancing sub-micron properties of nanocomposites with extremely small grain size (<50 nm). The reason for substantial research in this area is to address the low friction and high wear resistance requirement of various industrial sectors [1,2].

Compared to conventional metallic materials, the addition of nano constituents in the metal matrix greatly enhances thermal, electrical, optical and mechanical properties [3–5]. A well-established low-cost, reliable and environmentally friendly method for the fabrication of nanocomposite coatings is electrodeposition, which normally involves electroless pulse coating deposition technique at ambient conditions [6, 7]. Various nano particles have been used for electrodeposition including Aluminium oxide, Silicon Carbide, Zirconium dioxide, Graphene and Titanium dioxide [7–11]. Recent studies have found that the frictional performance of electrodeposited nickel Graphene (Ni/GPL) was better as compared to nickel- Aluminium oxide, nickel- Silicon Carbide, nickel- Zirconium dioxide [12,13]. A high volume of

Nomenclature

u	Sliding velocity (μm/s)
η	Viscosity of bulk lubricant Ns/m^2
V_W	Wear volume (μm^3)
$\sum W_d$	Dissipated friction energy (Nm)$\sum W_{dh}$Energy distribution (Nm/m^2)$h_{oil\infty}$ Dissipated friction energy (Nm)$\sum W_{dh}$ Energy distribution (Nm/m^2)$h_{oil\infty}$Thickness of the oil in vicinity of the contact (μm)
μ	Coefficient of friction
a_H	Half width of the Hertzian contact (μm)
$a_{(i)}$	Half width of the contact at the *i*th fretting cycle (μm)
h(x)	Wear depth at the *x*position of the interface (2D contact) (μm)
$h_{(i)}$ (x)	Wear depth at the *x* position of the interface (2D contact) at the *i*th fretting cycle (μm)
K_v	Archard wear coefficient related to the wear volume analysis (μm3 (N m)$^{-1}$)
L	Axial length of the ball/coating contact (μm)

N	Fretting cycle related to the coating failure
P	Normal force (N)
$P_{(i)}$	Normal force during the ith fretting cycle (N)
P_L	Normal force per unit of axial length (2D contact) (N/mm)
P	Mean pressure (MPa)
δ_0	Residual displacement (μm)
δ	Displacement amplitudes (μm)
δ_g	Sliding distance (μm)
Q	Friction force (N)
D_p	Grain size at the time of coating deposition (μm)D_{max}Grain size after wear deformation (μm)k_sSurface permeability of coatingþ and m Grain size at the time of coating deposition (μm)D_{max}Grain size after wear deformation (μm)k_sSurface permeability of coatingþ and mMaterial properties

γ_sStress sensitivity coefficientAbbreviations

CTE	Coefficient of thermal elastic mismatch
SD	Starvation degree

experimental research has been conducted for in-depth understating in terms of comparison of frictional performance of various nanocomposite coatings. But less effort has been put in the development of predictive models to investigate nanocomposite coatings Coefficient of Friction (COF).

For the past few years, COF has been the focus of research in the area of structural reliability [14–16]. It is now possible to predict the COF in various metallic materials and alloys. Predicting the COF of nano-composite coatings is still a challenge due to its dependence on multiple cross-disciplinary parameters including: i) wear parameters, ii) intrinsic microstructural parameters such as porosity, surface stress, grain size and iii) lubrication parameters. Recent study shows a rising attentive-ness in enhanced wear and frictional modelling [17–21].

In this research, a 2D predictive model has been developed for nanocomposite coatings which incorporate the fretting wear, micro-structural and lubrication concepts for computing the Eigen stress-dependent oil-bath fretting wear procedures. The gross slip fretting conditions focusing on metal interfaces have been used which include failure, mainly due to abrasion. Similar research on nanocomposite coatings has been conducted in our centre [13,22–36]. This research answers the following vital questions using the concept of cross-disciplinary approaches. (i) How the standard frictional perfor-mance of nanocomposite coating and steel tribo-pairs can be charac-terised by fretting wear equations integrated with microstructural and lubrication formulae ? (ii) What measures can be taken to investigate the effects of essential microstructural parameters of the nanocomposite coatings on the COF ? (iii) What actions are required to predict the COF, similarly which intrinsic microstructural parameters influence COF the most ? and (iv) What procedures can be adopted to justify the reliability of COF predictions ?

2. Experiment

2.1. Sample preparation

Pulse electrodeposition method was used to deposit nanocomposite Ni/GPL coating of 0.04 μm surface roughness and 10 μm thickness on to a steel disc sample of 30 mm by 10 mm by 3 mm. For repeatability, three samples were used in each test. Proper surface conditioning using ul-trasonic treatment was performed on each sample before the deposition of coating. For electrodeposition, the bath solution was prepared with NiSO$_4$(H$_2$O)$_6$ of 210 g/L, NiCl$_2$ of 52 g/L and H$_3$BO$_3$ of 32 g/L. The Graphene nanoparticles were used with concentration of 15 g/L and

particle size of 8–9 nm. To avoid agglomeration, ultrasonic dispersion method was used to disperse nanoparticles in a bath solution. To ensure that the particles were homogeneously suspended in the bath solution, the magnetic stirrer was continuously used for 15 h before the start of experiment. The pH of solution was maintained in between 2.5 and 3.0 by using NaOH and diluted H$_2$SO$_4$. The following attributes are kept unchanged through the experiment: current density as 7 A/dm^2, on-off pulse time to 20–80 ms and with a duty cycle as 25%. Pure nickel and Steel disc were used as anode and cathode respectively.

2.2. COF tests method

COF tests of Ni/GPL samples were conducted by using precise reciprocating sliding wear Tribometer (Fig. 1). A horizontal displacer persuaded reciprocating motion at 10 Hz of constant frequency and 0.1 m/s of sliding velocity. For simulating the ball-on-disk using oil lubri-cation condition, the counter 100Cr6 steel ball (H: 520HV, E: 210 GPa, υ: 0.31 with a radius R = 22.5 mm) was used in tribo-contact with a lower fixed Ni/GPL sample. Prior to testing, the Ni/GPL samples were conditioned with acetone. Next the zero-reference of normal force was computed. The samples were than subjected to the oil into bath till a thin film was generated on the bottom flat sample. The required force was applied on to sample after introducing it to point contact.

For comparative study, the friction behaviour of pure Nickel (Ni) coating under various test conditions (Table 1) was also examined. The intention of choosing Nickel coating for comparative study is, that its substantial use in various industries such as bearing and its enhanced frictional properties relative to some wear-resistant materials [37].

The experiments were conducted at 40 °C using two different vis-cosity oils (mineral) i.e.10 cSt and 70 cSt. Base oils without any additives were used, to make sure that they perform the same, once the system approaches the stable-state between the replenishment stage and removal stage of the oil from the contact. During the whole period of test, the coated samples were completely immersed in about 2 mm layer of oil. The frictional force (Q) and displacement amplitude (δ) were continuously logged while maintaining the normal force (P) constant. The frictional force was used to compute the COF as a function of number of cycles. The fretting test programmes were performed in accordance with the conditions mentioned in Table 1 and every test was duplicated in order to confirm accuracy. All tests were conducted in a sealed chamber with well-controlled temperature and relative humidity as mentioned in Table 1.

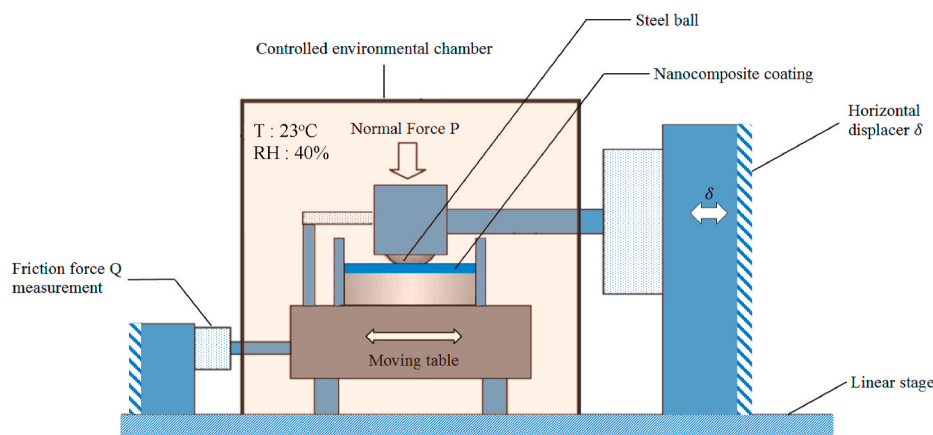The system compliance of the tribometer was carefully considered in

Fig. 1. Schematic diagram of sliding retting Tribometer with controlled environmental chamber [33].

Table 1
COF test conditions for fretting test under oil bath lubrication condition.

Variable Parameters					
Test 1	Lubricant viscosity (η)	10 cSt	70 cSt		
Test 2	Displacement amplitudes (δ)	±60 μm	±80 μm	±100 μm	±120 μm
Test 3	Maximum linear force (P)	10 N	40 N		
Test 4	Grain sizes (Dp)	10.08 ± 6 nm	23.08 ± 4 nm		
Constant Parameters					
	Relative Humidity (RH)	40% ± 5%			
	Temperature (T)	23 °C ± 3 °C			
	Maximum number of cycles (N)	70,000			
	Frequency	5 Hz			
	Counter steel ball radius (R)	22.5 mm			

order to get reliable displacement values at the interface. Therefore, for same displacement δ, various different interface sliding could be produced, subject to the accuracy of tribometer. Such situation was avoided by continuous monitoring of fretting log by maintaining constant residual displacement δ_0 during the whole period of experiment. To properly define the displacement amplitude, the friction force was kept zero (Q = 0), though there is no effect of the accuracy of tribometer on friction force. The comparison of test results was performed without considering the regime of test system. This study was conducted for high gross sliding conditions, in order for the residual contribution to be comparable to fretting sliding distance ($\delta_g = \delta_0$). The contribution of 'N' fretting cycle is added i.e. $\sum W_d = \sum_{i=1}^{N} W_{(i)}$ to compute the interfacial shear work at the interface W_d (also known as accumulated dissipated energy).

2.3. Experimental observations

2.3.1. Pre-tests observations

Pre-test grain size measurement info-graphs revealed that Ni exhibited larger grain size of 23.08 ± 4 nm (Fig. 2 (b)) compared to Ni/GPL grain size of 10.08 ± 6 nm (Fig. 2 (a)). Grain size substantially effects the frictional properties of nanocomposite coatings [38]. Cross-sectional SEM images of both coatings were used to analyze the pre-test particle size and distribution (Fig. 3) showing the graphene particles in Ni/GPL are uniformly distributed in huge amount compared to pure Ni. The more magnified SEM images of coatings surface in Fig. 3 show the surface morphologies of Ni/GPL and pure Ni coatings. It can be

clearly observed that the Ni/GPL coating has a smooth surface with finer grains than the pure Ni coating. It has already been reported [38] that codeposition of graphene nanoparticles in Ni causes reduction of grain size due to the inhibition of regular grain growth and enhancement of fresh nucleation caused by second phase particles. Fig. 4 show the AFM observation of surface morphology of the Ni/GPL and Ni. The Ni coating showed larger and dissimilar grains. The incorporation of graphene nanoparticles in nickel matrix modified the electro-crystallization mechanism leading to smooth and homogeneous surface morphology. This is also evidenced by significantly lower surface roughness value of Ni/GPL coating as compared to pure nickel coating. Pre-Test EDS elemental analyses of both coatings are shown in Fig. 5. Spectroscopic peaks of graphene (C) confirmed its influence on tribological properties. Ni/GPL composite shows the higher peak of graphene element as a direct result of homogeneous graphene particles distribution in the coating.

2.3.2. COF test

All the results of the COF tests (mentioned in Table 1) show that the COF for Ni/GPL nanocomposite and pure Ni coatings depends on microstructural properties (for example hardness, grain size), properties of base oil lubricant (such as lubricant viscosity) and loading conditions (such as displacement amplitude and maximum linear force) [39]. Next sub-sections (2.3.1.1–2.3.4.1) will discuss the COF results for all the tests performed on Ni/GPL and Ni coatings.

2.3.2.1. Effect of various lubricant viscosities (η) – test 1. For Ni/GPL (Fig. 6 (a)), it was observed that for the similar mechanical conditions, the running-in period finishes faster for lower viscosity oil η = 10 cSt since lower viscosity oil provides good replenishment ability and less time (meaning number of cycles) is required to form a stable tribo-film [40]. Furthermore, the higher viscosity oil η = 70 cSt, did not form the stable tribo-film and also after few hundred cycles it deteriorated and additional time was required to recuperate the tribo-film. A similar phenomenon was also observed for the case of pure Ni (Fig. 6 (b)), however, the only difference was that the COF for both low and high viscosity oils for Ni was higher compared to the respective COF for low and high viscosity oil for Ni/GPL. The higher COF of Ni compared to Ni/GPL for both viscosities is associated with the micro-delamination behaviour of Ni creating wear debris thereby increasing the COF [41] (discussed in detail in next section 2.3.3). Ni/GPL exhibited lower COF since a substantial quantity of graphene within Ni/GPL caused the formation of a thick tribo-film composed of graphene (SEM micrograph shown in Fig. 6 (a)) thus improving the replenishment capabilities of the oil; consequently, the COF is reduced.

2.3.2.2. Effect of various displacement amplitudes (δ) – test 2. For Ni/GPL
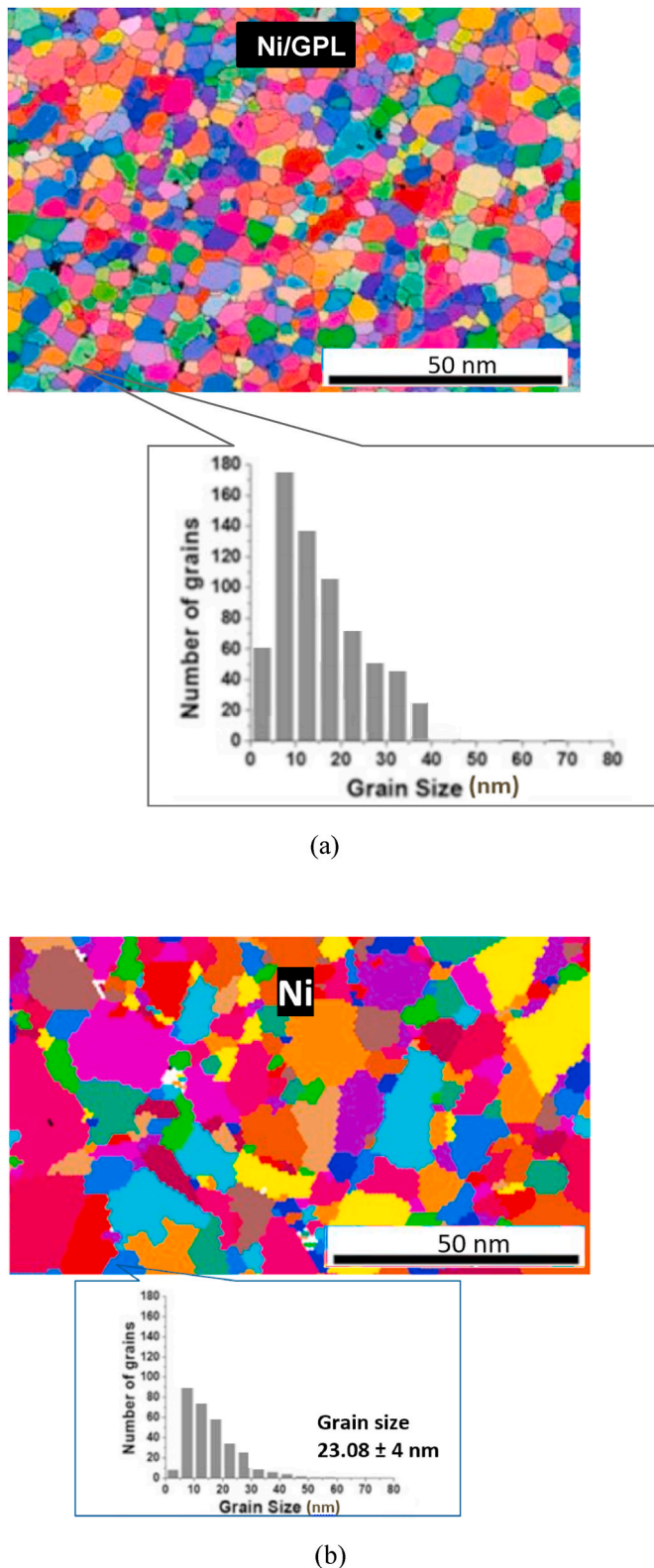
(a)

(b)

Fig. 2. Pre-test grain size info-graphs for (a) Ni/GPL (b) Ni.

with low viscosity oil $\eta = 10$ cSt condition, it becomes hard to distinguish the border between the running-in period and the steady state, especially for smaller values of sliding amplitudes as shown in Fig. 7 (a) [42]. However, for Ni, running-in and steady-state regime are distinguishable by a border as compared to Ni/GPL as shown in Fig. 7 (b). For Ni/GPL at smaller amplitudes, although, it is extremely difficult to

segregate the running-in period from the steady-state period, however, it is very important to separate the two distinct wear regimes for the sake of further investigation. This friction behaviour of Ni/GPL compared to Ni can be justified from the fact that Ni/GPL has comparatively large hardness value due to its refined and compact grain structure (Fig. 2), thereby minimising the difference between running-in and steady regimes due to almost stable continuous friction behaviour.

For both Ni/GPL and Ni, it was observed that the running in period becomes shorter with increasing displacement amplitude. For example, for Ni with smallest displacement amplitude at 60 μm, the running-in period lasted 6×10^3 cycles followed by 5.5×10^3 cycles at 80 μm, 5 $\times 10^3$ cycles at 100 μm and finally 4×10^3 cycles at 120 μm. Following this, a stable and steady state was observed. Similar friction response for running-in period was observed for Ni/GPL having shorter running-in period for highest displacement amplitude and vice versa. However, the comparison between the running-in periods for Ni/GPL and Ni shows that Ni has slightly longer running-in periods compared to Ni/ GPL for all displacement amplitudes. The reason, for shorter running-in periods, for Ni/GPL compared to Ni is that Ni/GPL develops a thicker layer of tribo-film which supports sliding under higher amplitude conditions [43].

2.3.2.3. Effect of various normal forces (P) – test 3. For low viscosity oil at $\eta = 10$ cSt, friction behaviour of Ni/GPL and Ni coatings is tested, under 10 N and 40 N, with continuous loading conditions as shown in Fig. 8(a–b). Both for Ni/GPL and Ni, the observed COF at initial 10 N normal force was lower than 40 N. At higher normal force ($>$10 N) the COF increases significantly. It can also be seen that when Ni/GPL was subjected to 40 N, the COF for Ni/GPL was still lower than the COF of Ni at 10 N as shown in Fig. 8(a–b). This means that although the COF of Ni/ GPL increases with increasing normal force, thereby reducing its performance, the COF of Ni/GPL corresponding to the highest normal force (40 N) was lower and better than the COF of Ni. This better friction behaviour of Ni/GPL compared to Ni can be justified based on the fact that Ni/GPL has comparatively higher hardness value attributed to its refined and compact grain structure (Fig. 2). In addition, better frictional behaviour of Ni/GPL is achieved due to the formation of thin uniform graphene protection/tribo-layer that contributes to reducing friction and wear at the interfaces of tribo-contact [44]. On the other hand, decreasing performance of Ni/GPL with increasing normal force is linked to depleting graphene (C) with the stepwise increase in normal force, resulting in the reduction of hardness of Ni/GPL causing micro-ploughing [45] as shown in SEM/EDS micrograph in Fig. 8 (a).

There was additional significant behaviour observed during the running-in stage of Ni/GPL. Running-in period for Ni/GPL gradually became shorter with increasing normal force compared to longer running-in period for Ni. The reason for gradual decrease in running-in period of Ni/GPL corresponding to increasing normal force was because of a thicker tribo-film which is required for better sliding compared to thin tribo-film at low normal force as shown in top SEM micrograph in Fig. 8 (a) [46].

Disturbances in the Ni/GPL COF curve at steady state were observed. These disturbances were larger for higher normal force, as additional energy is required to heal the tribo-film due to micro-ploughing (see Fig. 8 (a)) [47]. On the other hand, during the steady state, the disturbance in the trend of Ni COF was far longer as compared to Ni/GPL. The reason for this can be attributed to debris production due to micro-delamination (see Fig. 8 (b)) and in turn more energy is needed to retain the tribo-film for Ni as compared to Ni/GPL.

2.3.2.4. Effect of various grain sizes (D_{max}) – test 4. Likewise, the effect of corresponding Ni and Ni/GPL grain sizes on COF is shown in Fig. 9. The COF was observed to be higher for Ni compared to Ni/GPL. This higher COF of Ni compared to Ni/GPL is related to larger grain size of Ni (Fig. 2) which results in micro-delamination behaviour, hence
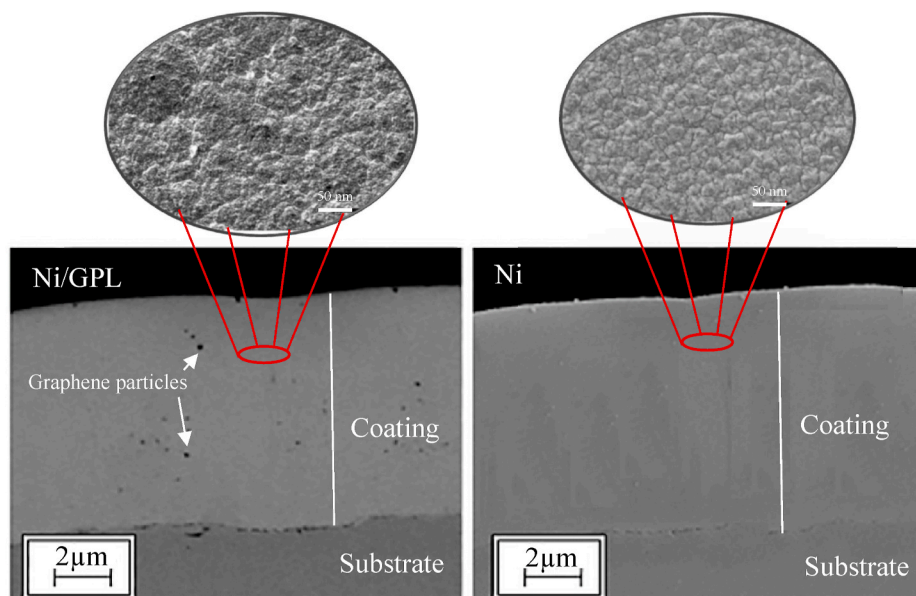
Fig. 3. Pre-test cross-sectional SEM micrographs of the nickel-based composite coatings for Ni/GPL and pure Ni.
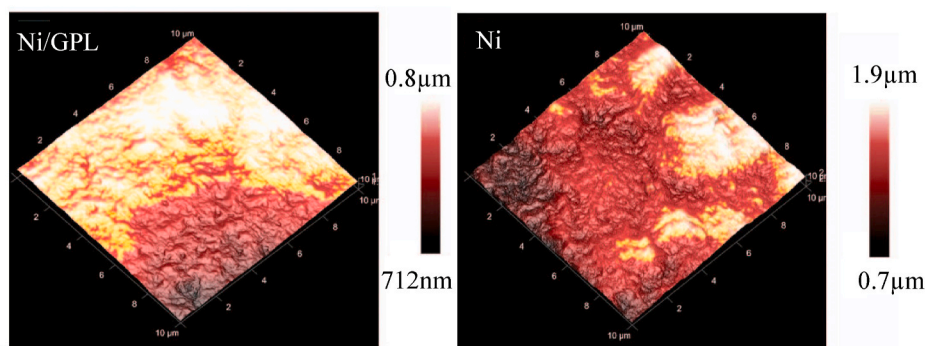

Fig. 4. Pre-test AFM images of surface morphology Ni/GPL and pure Ni.
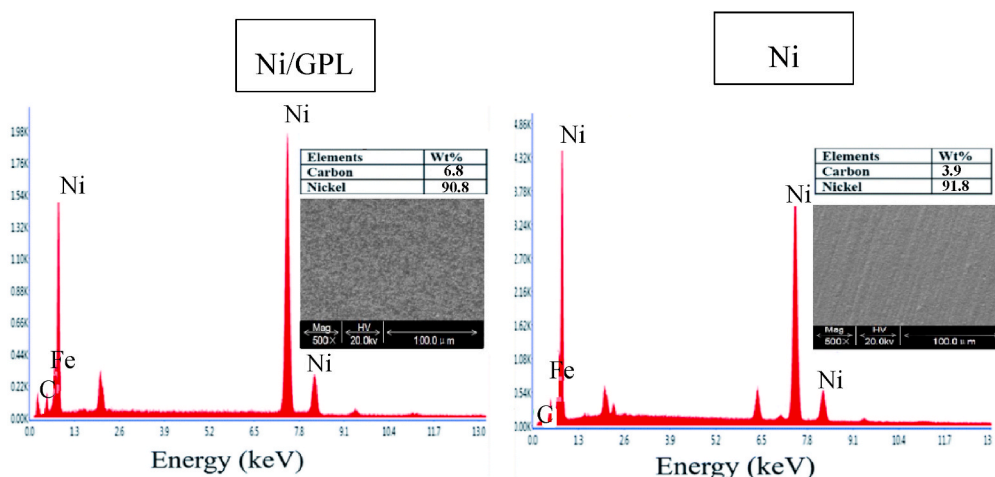

Fig. 5. Pre-test EDS micrographs of the nickel-based composite coatings for Ni/GPL and pure Ni.

producing increased wear debris with the increased COF as evident from previous SEM images and ref. [21]. Fig. 9 shows COF for both coatings as a function of the number of stress cycles exhibiting a clearer stability in the COF beyond specific point. The running-in period of Ni/GPL is around only 2×10^3 cycles as compared to Ni which is around 4×10^3 cycles. Ni/GPL showed shorter running-in period and lower COF because of the smaller grain size resulting in lower surface roughness which in turn results in lower COF. Significant quantity of graphene in
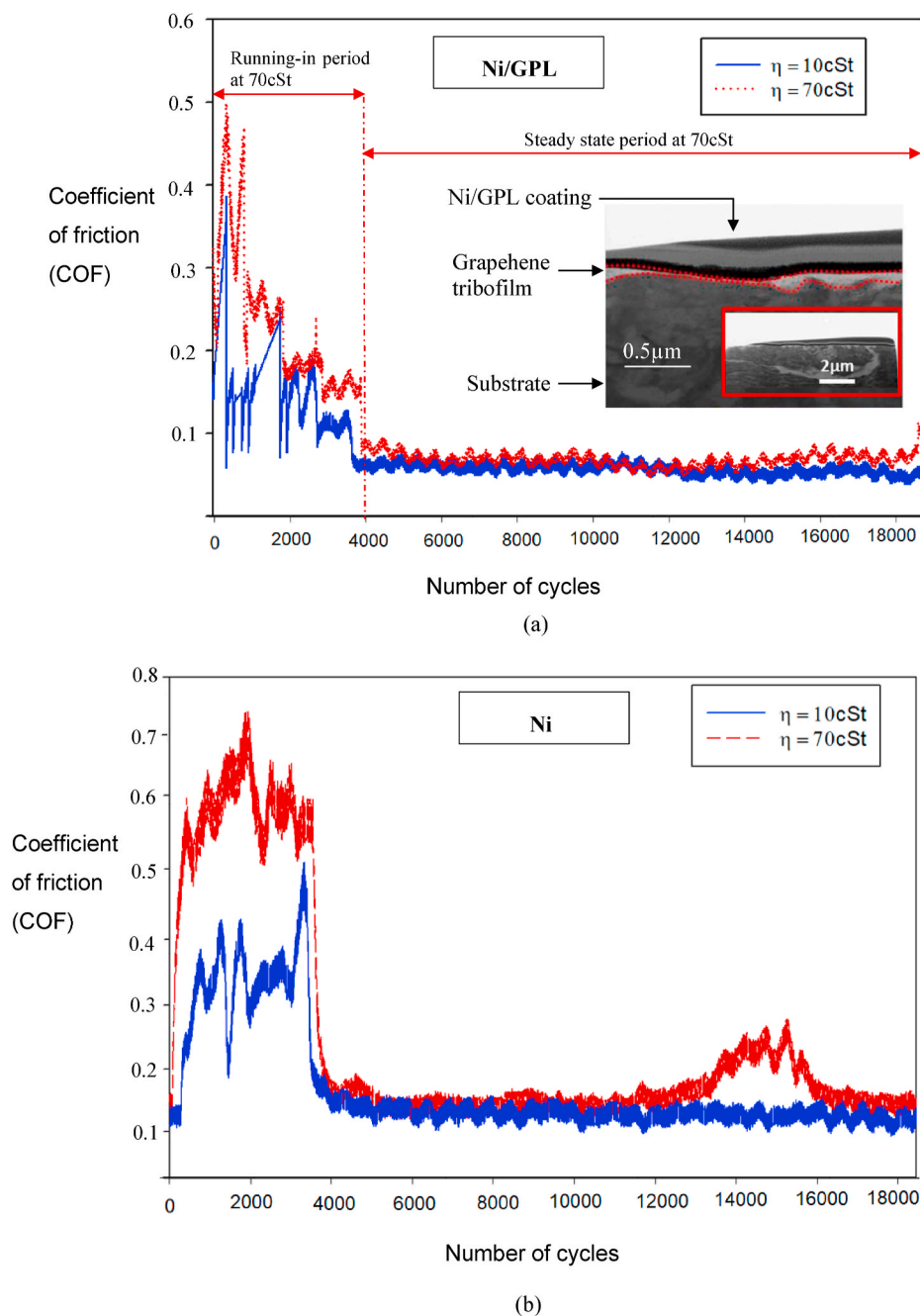
Fig. 6. The schematics for (a) Ni/GPL and (b) Ni showing the effect of the oil viscosity (η) on frictional behaviour of the interface for $\varphi = 28.64$ mm, P0H = 2.00 GPa, Ra = 0.032 μm, δg = 100 μm.

Ni/GPL caused the development of graphene tribo-film; therefore, resulting in shorter running-in period and lower COF.

2.3.3. Post tests observations

The post-test EDS micrographs in Table 2 identify the elements and their concentration for Ni/GPL and Ni samples that underwent Test 4 conditions: $\eta = 10$ cSt, $\varphi = 28.64$ mm and Ra = 0.020 μm and P0H = 10 N. EDS was performed for Ni/GPL and Ni at least five spectral points inside and outside the wear tracks, but for demonstration, only one spectral point inside and one outside point are shown. Inside spectral points were used to compare the percentage weight loss of elements inside the wear tracks from outside. EDS results showed that Ni showed larger percentage weight loss of elements inside the wear tracks compared to Ni/GPL.

The comparison of the EDS results for Ni/GPL and Ni showed a higher percentage of Ni weight loss in the wear tracks of Ni samples compared to Ni in the wear tracks of Ni/GPL samples. For example, the percentage weight loss of Ni in Ni sample was 40% compared to 20% loss of Ni in Ni/GPL sample. The lower percentage weight loss of Ni/GPL sample compared to Ni sample is linked with its microstructural properties [48]. Ni/GPL contains refined grains (as shown in Fig. 2 (a)), which minimizes the transfer of corrosive contaminants, water and oxygen, therefore preventing coating from severe fractures, oxidation and grain extraction during wear cycles. This behaviour of the Ni/GPL sample resulted in a slight percentage weight loss compared to the Ni sample during the tribo experiment.

Another interesting result from EDS is the higher weight percentage of carbon in the corrosion paths of the Ni/GPL sample compared to the
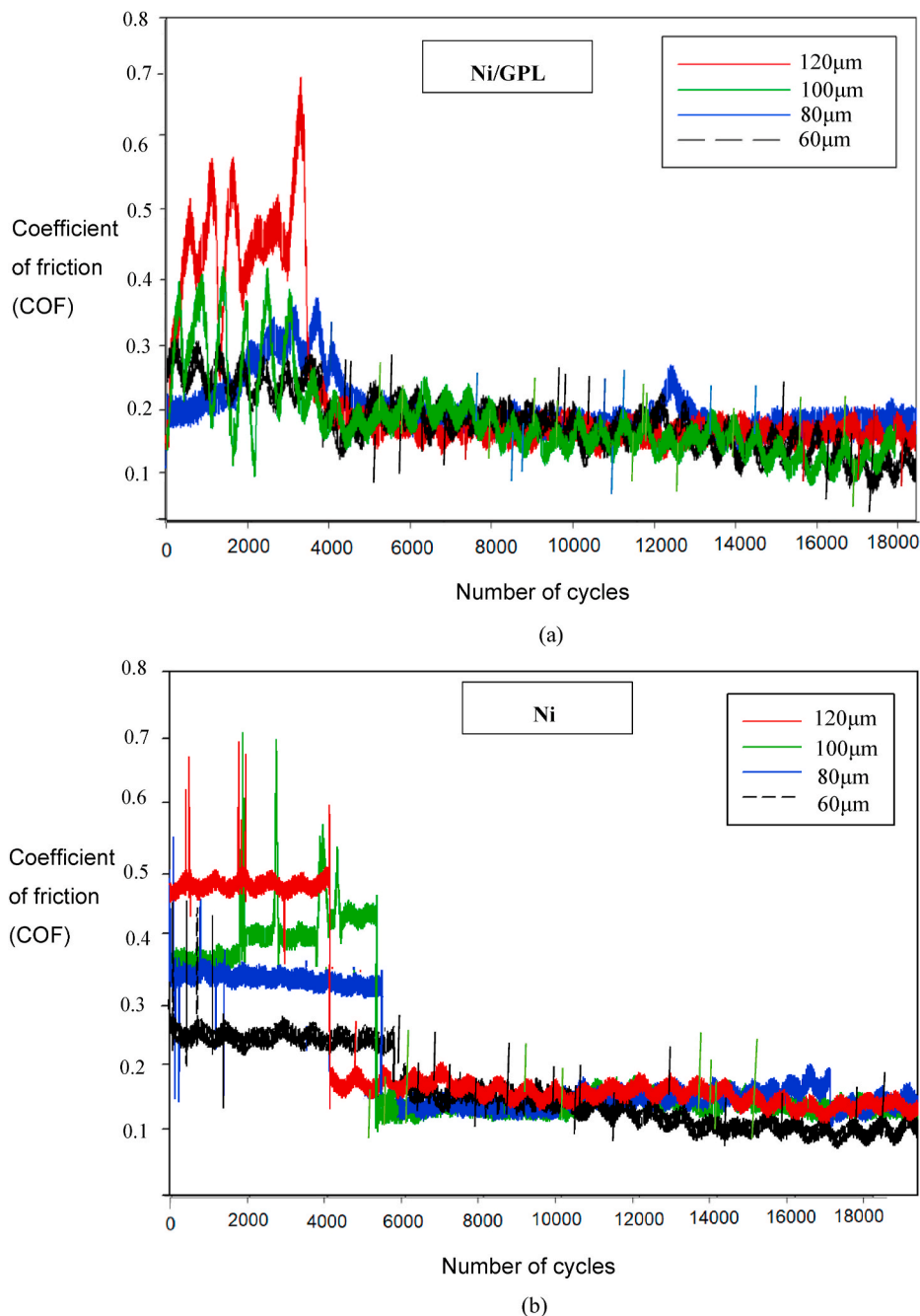
(a)

(b)

Fig. 7. The schematics for (a) Ni/GPL and (b) Ni showing effect of 4 different sliding amplitudes on frictional behaviour for η = 10 cSt), φ = 28.64 mm, Ra = 0.020 μm and P0H = 10 N.

nickel sample. This is because in Ni/GPL wear paths, some of the carbon comes from the decomposition of carbon chains in graphene and a significant amount of the carbon comes from the wear of the counter carbon steel ball. The surface of the counter carbon steel ball that slided against the Ni/GPL sample showed a large wear weight loss (Fig. 10 (a)) compared to the Ni sample (Fig. 10 (b)).

This indicated that the hardness (480 HV) of Ni/GPL is slightly closer [49] to the hardness (520 HV) of counter carbon steel ball [50] compared to the hardness (266HV) of Ni [51]. Sliding wear response of both coatings in terms of hardness can also be justified by analysing the width of their wear tracks. The width of wear tracks for Ni/GPL and Ni were investigated by using SEM, as shown in Fig. 11(a–b). It is evident from SEM images that Ni/GPL exhibited 0.472 mm (Fig. 11 (a)) wide wear track compared to 0.812 mm (Fig. 11 (b)) of Ni, confirming that

the high hardness of Ni/GPL compared to Ni resulted in less wear weight loss of Ni/GPL.

Further, the moving average COF and corresponding wear volumes (V) was analysed for both Ni/GPL and Ni samples that underwent Test 4 conditions: η = 10 cSt, φ = 28.64 mm and Ra = 0.020 μm and P0H = 10 N. The rising trends of COF for both coatings were observed as a result of rising number of wear cycles and Archard loading factor W as shown in Fig. 12. Archard factor (aka. total dissipated energy during wear cycles) is equal to the product of normal force (P) and total sliding displacement (δ). Accordingly, the accumulated Archard factor ($\sum W$) is given by Ref. [52]:

$$\sum W = \sum_{i=1}^{N} W_{(i)}(Nm) \text{ where } W_{(i)} = 4 \, \delta g_{(i)} P_{(i)}(Nm) \tag{1}$$
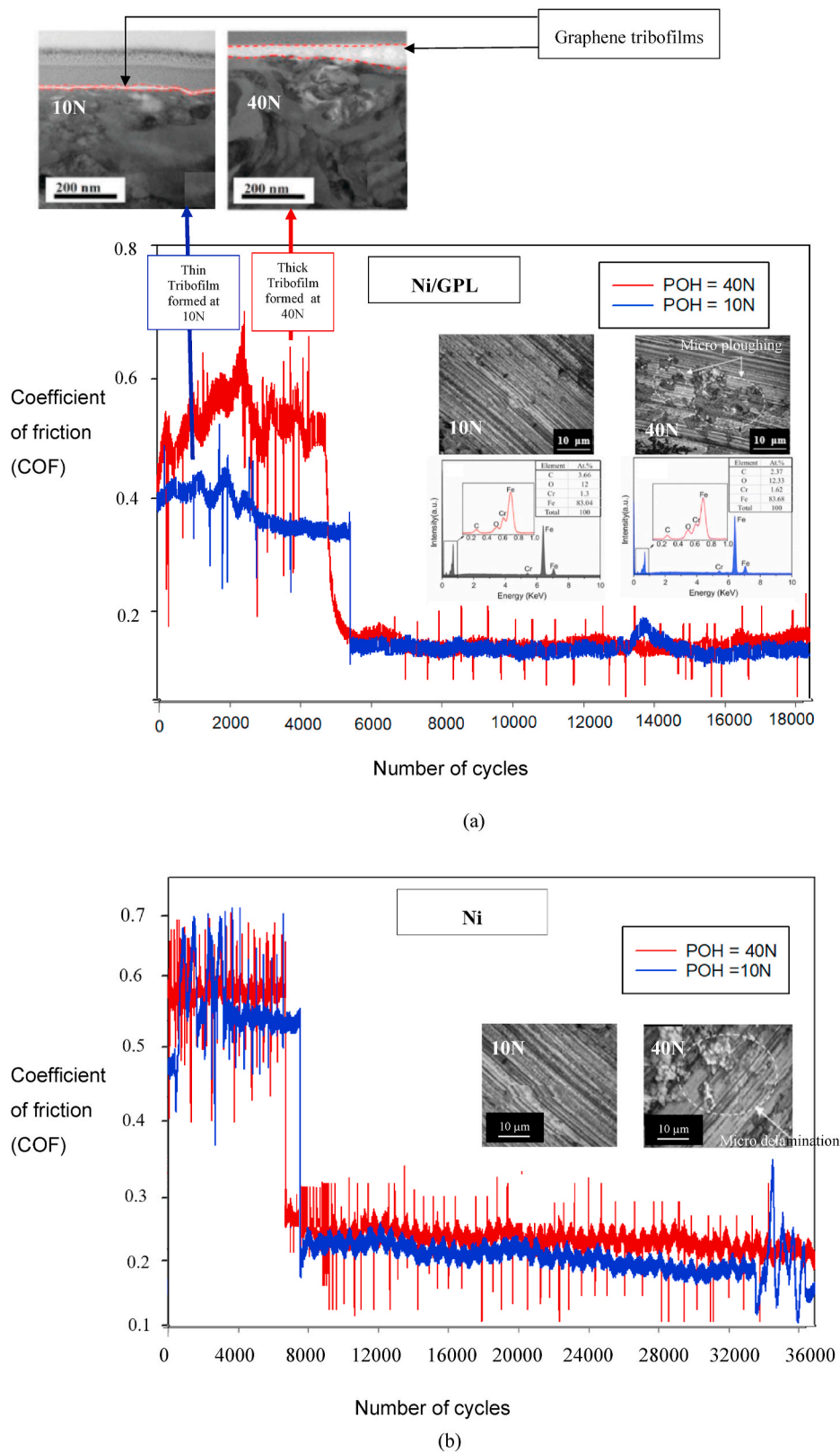
Fig. 8. The schematics for (a) Ni/GPL and (b) Ni showing effect of 2 different normal forces (POH = 10 N and 40 N) on frictional behaviour for $\eta = 10$ cSt, $\varphi = 28.64$ mm and Ra = 0.020 μm.

$W_{(i)}$ represents the Archard factor dissipated at the ith wear cycle.

The corresponding number of wear cycles (*i*) in Fig. 12 indicate that running-in period of Ni/GPL and Ni is around 2×10^3 cycles and 4×10^3 cycles respectively. These cycles revealed that the COF of both coatings stabilized with time, but as expected, Ni was noted to have quite a high COF compared to Ni/GPL.

In Fig. 12, wear volumes (V) for Ni/GPL and Ni show linearly rising trends. It is noteworthy, that for both coatings, the moment when
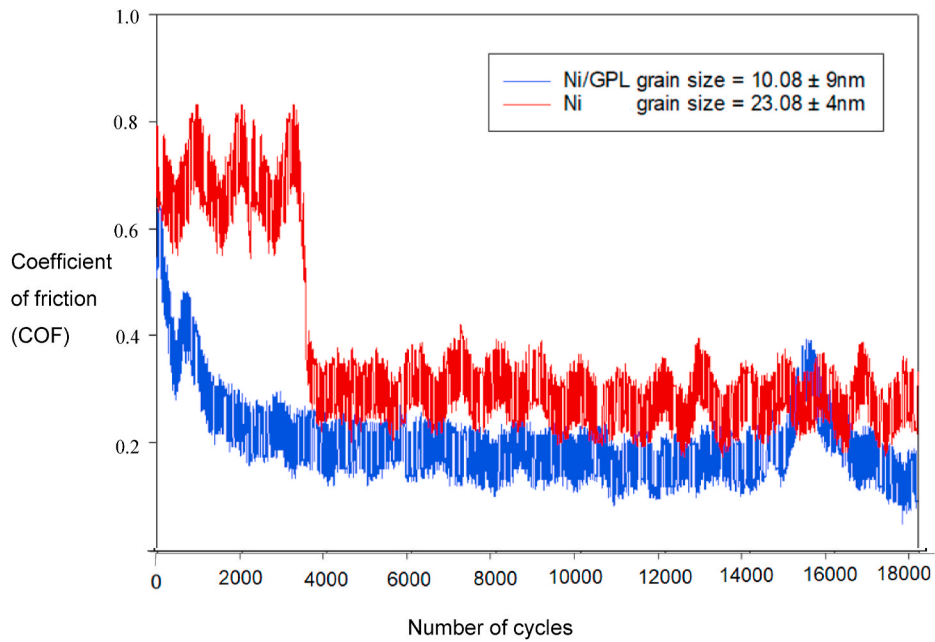
Fig. 9. The schematics for Ni/GPL and Ni showing the frictional behaviour of two nanocomposite coating due to their grain sizes for η = 10 cSt, φ = 28.64 mm and Ra = 0.020 μm and P0H = 10 N.

Table 2
Post-test EDS micrographs of Ni/GPL and Ni samples to determine the element type and concentration under base oil viscosity of η = 10 cSt.

running-in period ends, the corresponding wear begins. By using a conventional Archard description, wear volume could be calculated from the COF and accumulated Archard factor ($\sum W$).

$$\Delta V = K_v \times \Delta \left(\sum W_{(i)} \right) \ (\mu m^3) \qquad (2)$$

Where K_v in eq. (2) is the energy wear coefficient, $\mu m^3/Nm$ and $W_{(i)}$
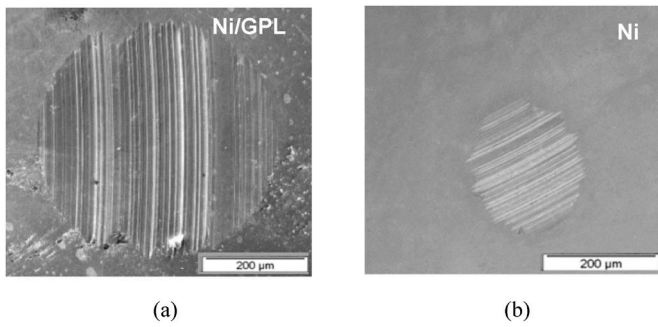
(a)   (b)

Fig. 10. The SEM micrographs of wear on counter carbon steel ball surface as a result of sliding against (a) Ni/GPL and (b) Ni under base oil viscosity of 10 cST.

indicates the dissipated Archard factor at the ith wear cycle

Wear volumes (V) in eq. (2) relates to normal force (P) with total sliding displacement (δ) as:

$$\Delta V = K_v \text{ x } \Delta \left(\sum 4 \, \delta g_{(i)} P_{(i)} \right) (\mu m^3) \tag{3}$$

Coulomb friction model, eq. (4) determines that the frictional force ($F_{(i)}$) is proportional to the applied normal load (P). Therefore, a COF (μ) is assumed to be constant, and after substituting eq. (4) in to eq. (3) a relationship between wear volume (V) and COF (μ) can be established, see eq. 5

$$F_{(i)} = \mu P_{(i)} (N) \tag{4}$$

$$\Delta V = K_v \text{ x } \Delta \left(\sum \frac{4 \, \delta g_{(i)} F_{(i)}}{\mu} \right) (\mu m^3) \tag{5}$$

As shown in Table 3, the normalised 'wear profiles' and 'wear depth kinetic profiles' for Ni/GPL and Ni are shown at different stages of wear degradation. It appeared that the wear profiles had a "U-shaped" behaviour with maximum wear depth often at the centre (x = 0). The normalised wear depth for Ni/GPL at i = 8,000[th] cycle is 0.39, whereas Ni showed a significantly higher normalised wear depth = 0.51. Interferometric surface measurements at various cycles are used to create the U-shaped wear profiles. The red profile shows a schematic wear profile for Ni/GPL at i = 8,000[th] cycle as an example of interferometric wear profile. The 3-D image of Ni/GPL and Ni interferometers at the i = 8000th cycle is shown in Table 3, which clearly shows that Ni/GPL exhibited less severe micro-ploughing deformation compared to severe micro-delaimation in Ni.

Using 3-D interferometric analysis at 8,000[th] cycle, it was observed

that Ni/GPL exhibited less severe micro-ploughing wear deformation than Ni which displayed severe micro-delamination. Based on corresponding wear profiles, Table 3 also shows the calculated wear depth kinetics $h_{(i)}(x)$ of Ni/GPL and Ni in different wear cycles. Wear depth kinetics profiles were developed using the incremental equation below:

$$h_{(i)}(x) \approx \frac{\Delta h}{\Delta i} = \frac{h_{(i)}(x) - h_{(i-\Delta i)}(x)}{\Delta i} \tag{6}$$

Where Δi is a single wear cycle.

The profile of normalised wear depth kinetics is significantly reduced in response to increasing cycles. For instance, at i = 8000th cycle the normalised wear depth kinetics of the Ni/GPL was 0.25 compared to Ni (0.06). Another interesting point is the evolutionary behaviour of the normalised wear depth kinetics profile. It starts with a Hertz shape, decreases to an elliptical shape, and eventually becomes a quasi-flat shape. Contact edges with a quasi-flat distribution (i = 8000th cycle and later) indicate the type of wear deformation. For instance, Ni/GPL micro-ploughing has a slight elevation in contact edges, while micro-delamination of Ni shows near perfect flat edges.

3. Modelling

A stepwise 2-D model for predicting COF is developed based on experimental analysis for the nanocomposite coatings. This model integrates the concept of "energy profile distribution of wear depth kinetics" presented in experiments with the microstructural and rheological parameters.

As our experiments show that COF depends on multiple cross-disciplinary parameters including lubricant viscosity, displacement amplitudes, maximum linear force and grain sizes. Therefore to address our aim for developing a predictive COF model, three modelling approaches have been integrated which include wear [21], microstructural [53] and lubrication [54,55] modelling as shown in Fig. 13.

3.1. Wear modelling

This section mainly includes results which are given in Ref. [56]. However, for proper understanding, some important points are recalled here.

Wear resistance of nanocomposite coating can be evaluated by using a linear expression which relates the wear volume, μm^3 (V) with and the accumulated Archard factor density, Nm ($\sum W_d$) and energy wear coefficient $\mu m^3/Nm$ (K_v) during the fretting cycles as [57],

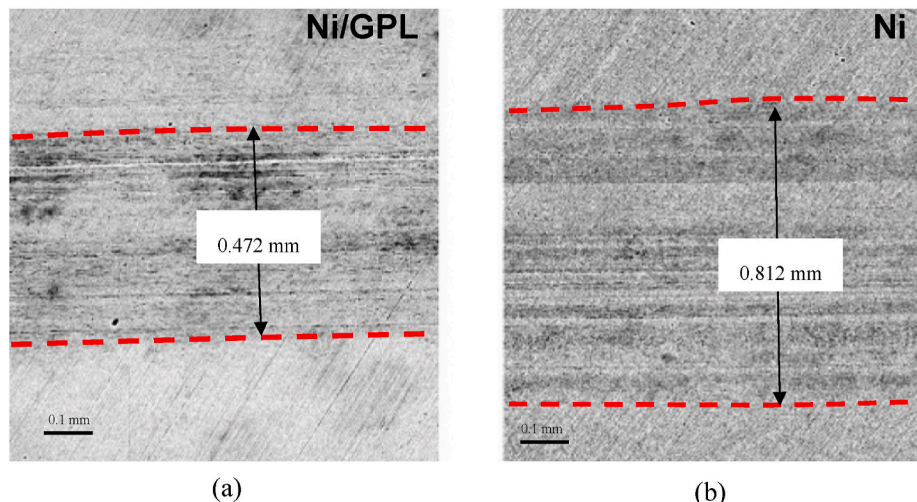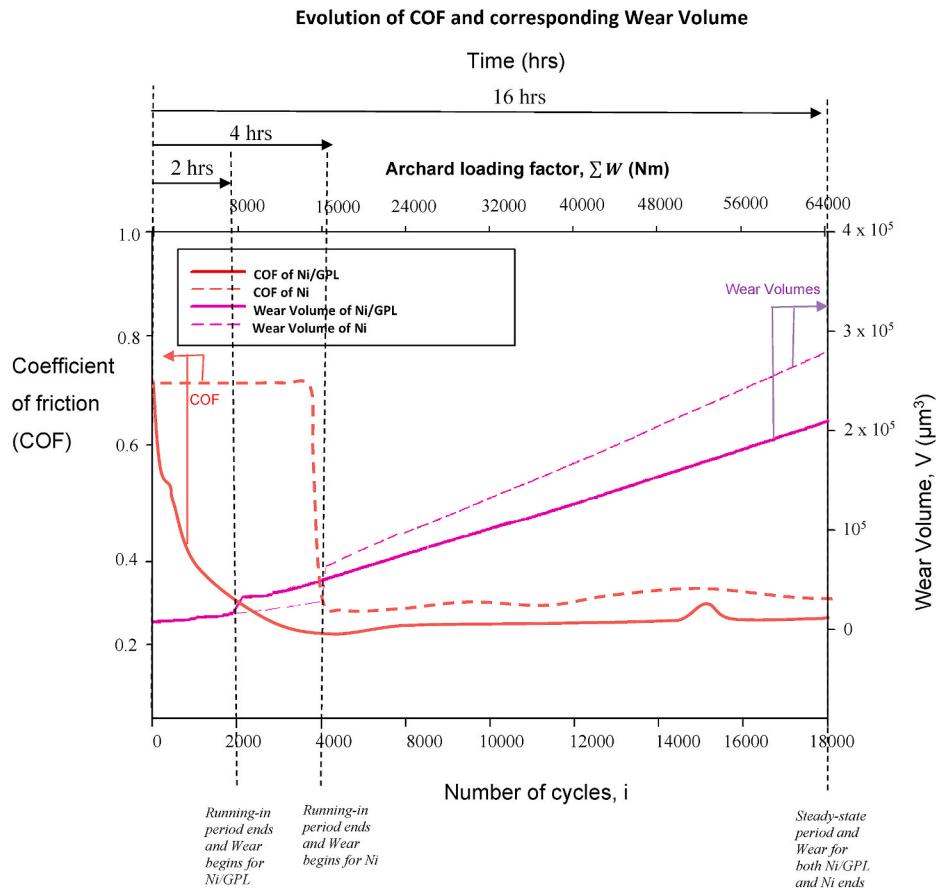(a)   (b)

Fig. 11. The SEM micrographs showing the width of wear tracks of (a) Ni/GPL and (b) Ni sliding against carbon steel ball under base oil viscosity of 10 cST.

Evolution of COF and corresponding Wear Volume

Fig. 12. The evolution of COF for both Ni/GPL and Ni for conditions: η = 10 cSt, φ = 28.64 mm and Ra = 0.020 μm and P0H = 10 N.

$$V = \sum W_d K_v \tag{7}$$

$$\sum W_d = \sum_{i=1}^{N} W_{(i)}; \quad W_{(i)} = \sum_{i=1}^{N} P(i)\delta_g(i) \tag{8}$$

It can be seen in eq. (8) that the dissipated Archard factor density $W_{(i)}$ during the ith fretting cycle is the multiplication of normal force (P) and

depth kinetics $h_{(i)}(x)$ [55].

The experimental studies presented here shows that the distribution of the Archard parameters becomes quasi-flat $W_{F(i)}$ after several hundred cycles (Table 3). During ith cycle, the flat contact formula for the dissipated Archard factor density at x = 0 is shown in the second part of eq. (9) on right [55].

$$\sum W_{(i)}(0) = \sum W_{H(i)=E(i)}(0) + W_{F(i)}(0) = \underbrace{\sum_{i=1}^{i_{ft}} \left[\frac{W_{(i)}}{\pi \delta g_{(i)} L} \left(\frac{\delta g_{(i)}}{a_{(i)}} \left(1 - \left(\frac{\delta g_{(i)}}{a_{(i)}} \right)^2 \right)^{\frac{1}{2}} + \arcsin\left(\frac{\delta g_{(i)}}{a_{(i)}} \right) \right) \right]}_{\text{Hertzian/Elliptical approximation}}$$

the entire sliding distance (δ_g) at that particular cycle as shown in Fig. 14 (a).

Coating durability is typically associated to the vertical wear loss. Therefore, compared to a conventional wear volume analysis, it is much reliable to use wear depth, μm (h) quantification for predicting the coating durability [36,58]. It, however, requires a local analysis. As seen from the experimental study that at the initiation stage of reciprocating wear cycles, the typical elliptical shape is displayed which after few hundred cycles reduces to Hertzian and eventually becomes quasi-flat shaped as shown in Fig. 14 (b). The equations of the Archard factor density $W(0)$ (N m/μm²) and accumulated Archard factor density $\sum W(0)$ were developed by correlating the maximum wear depth h(0) (μm) at the wear scar centre (i.e. x = 0) in relation to the corresponding wear

$$+ \underbrace{\sum_{i=i_{ft}}^{N} \left[\frac{W_{(i)}}{2a_{(i)} L \left(1 + \frac{\delta g_{(i)}}{2a_{(i)}} \right)} \right]}_{\text{Flat approximation}} \tag{9}$$

$W_{(i)}$ and $a_{(i)}$ represent the Archard factor and contact radius of the ith cycle for hertzian, elliptical, and flat contacts. At a given normal force applied P, Archard's density $W_{H(i)=E(i)}(0)$ method assumes that relative sliding $\delta g_{(i)}$ remains lower than the contact radius $a_{(i)}$.

For the ith wear cycle, $a_{(i)}$ is given as [55],

Table 3

Wear depth profiles for the various ith wear cycles of Ni/GPL and Ni, as well as 3-D interferometry images showing the type of delamination due to wear. The table also shows the wear depth kinetics profiles corresponding to wear profiles depths for various Ni/GPL wear cycles.
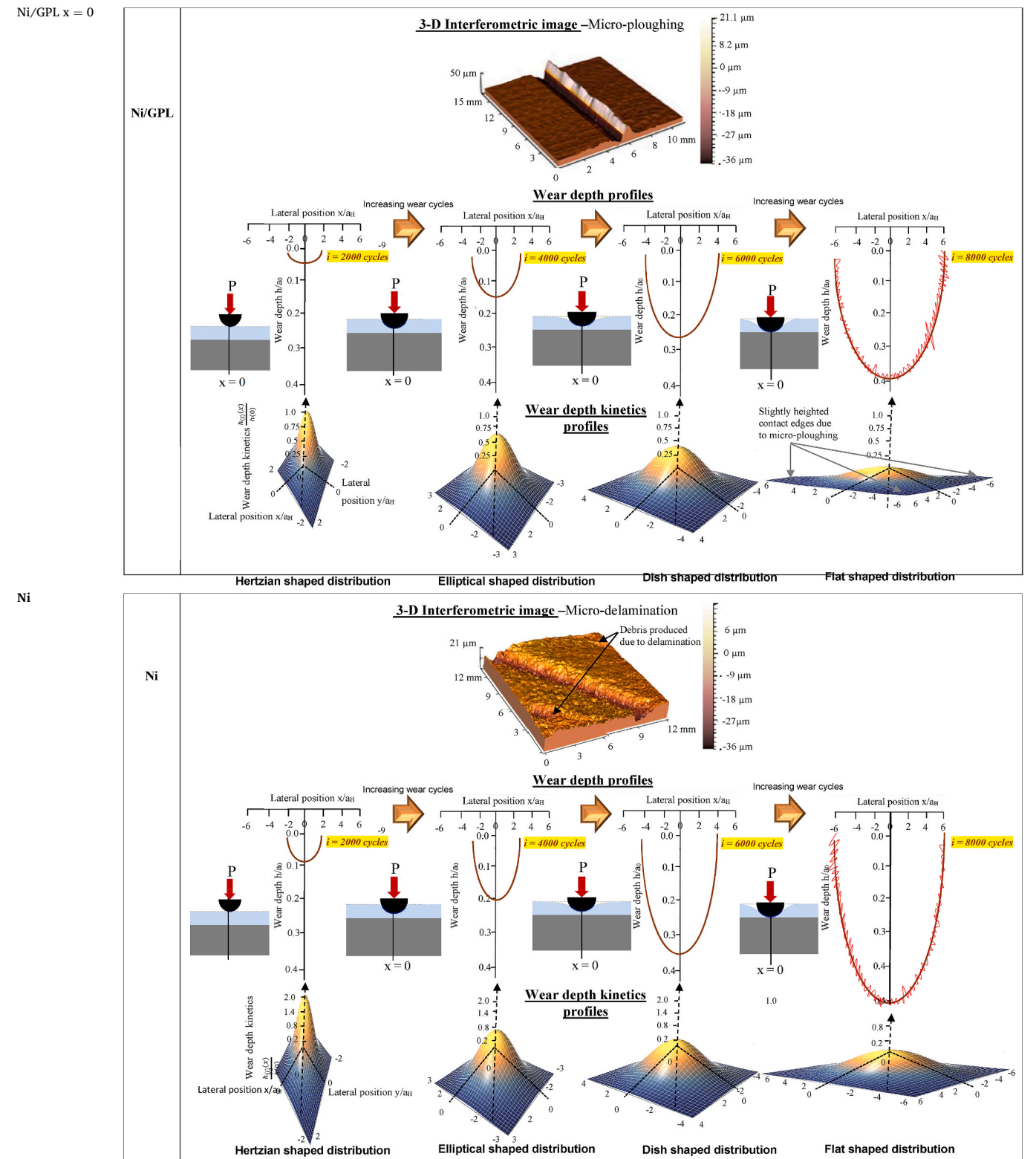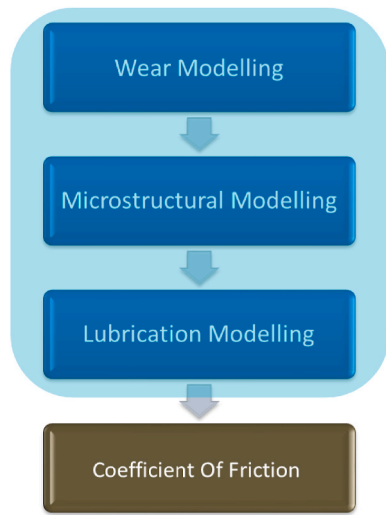
Fig. 13. The stepwise modelling approach for predicting COF for the nano-composite coatings.

$$D_{max} = D_p + \sqrt{\frac{\left[1 - \left(\gamma_s e^{-\frac{\sigma_c(0)}{E_1}}\right)\right]^2 k_s}{\left[\gamma_s e^{-\frac{\sigma_c(0)}{E_1}}\right]^3}} \tag{12}$$

Where, D_p denotes the grain size when coating is initially deposited while D_{max} is the grain size post wear deformation. $k_s = þP_s^m$ is the surface penetrability of coating; The terms: $þ$ and m denote the material properties. The coating develops residual stress $\sigma_c(0)$ at the interface, if during wear test, the coating-substrate system which have CTE mismatch, encounters the change in temperature ΔT from the temperature at which coating was initially deposited [56,63].

Eq. (13) is assumes that during the wear deformation, the particles and grain boundaries could not be separated.

Now, as the grain size increases the surface roughness of nanocomposite coating also increases. This estimation allows to assess the limiting strains based on coating thickness, surface roughness and grain size. The equation below was acquired experimentally [53],

$$R_S = YD_{max}\overline{\varepsilon_d} + R_o \text{ and } h = h_B + 2R_s \sin\theta \tag{13}$$

Where, R_S (shown in Fig. 16) is the surface roughness/asperities present

$$a_{(i)} = \frac{4PR}{\pi L}\left(\frac{1 - v_1^2}{E_1} + \frac{1 - v_2^2}{E_2}\right)\begin{cases} if\ a_{(i)} < a_{ft}\ and\ i < i_{ft} & then \sum W(0) = \sum W_{H(i)=E(i)}(0) \\ if\ a_{(i)} > a_{ft}\ and\ i > i_{ft} & then \sum W(0) = W_{F(i)}(0) \end{cases} \tag{10}$$

Where, a_{ft} and i_{ft} are the critical contact radius and critical cycle respectively, R is the ball radius, L is the axial length of the ball/coating contact, v_1 and v_2 are the coating and ball Poisson's coefficients respectively and E_1 and E_2 are the coating and ball Young's modulus respectively.

If the degradation ($a_{(i)} < a_{ft}$) and cycle ($i < i_{ft}$) are less than a critical point, the Archard factor density value is determined by the elliptical/hertizian approximation, while if they are higher, the flat approximation is used.

It can be seen in eq. (11) that the coating's Young's modulus E_1 is dependent on the coating surface porosity P_s and coating surface stress σ_c (0) which is given as: [59].

$$P_s = \gamma_s \exp\left(-\frac{\sigma_c(0)}{E_1}\right) \tag{11}$$

$$\sigma_c(0) = E_1\left(\frac{(E_3\alpha_s s + E_1\alpha_c h_c(0))\Delta T}{(E_3 s + E_1 h_c(0))} + \frac{x - t_b}{\zeta_r} - \alpha_c\Delta T\right) \tag{11a}$$

Where in eq. (11) (a), σ_c (0) is surface stress of coating (biaxial) at the middle of wear scar (interface) illustrated in form of Hooke's law in eq. (11) (a); γ_s is the stress sensitivity coefficient [60]. The coating surface develops the residual stress due to temperature changes ΔT from the fabrication temperature, if coating's CTE (α_c) is different from the substrate's CTE (α_s). Where E_1 and E_3 in eq. (11) (a) are the Young's moduli of coating and substrate respectively. The terms: h_c (0), t_b and ζ_r denote the coating thickness at the middle of wear scar, bending axis position and the curvature radius of coating-substrate system as a result of residual stress [61] respectively.

3.2. Microstructural modelling

It is important to note that the nanocomposite coating's Young's modulus E_1 (in eq. (12)) is related to extrinsic residual stress σ_c (Fig. 15) at the middle of wear scar and the coating's mean maximum grain size D_{max} (diameter) as [56,59,62].

at the effective strain $\overline{\varepsilon_d}$ during wear; R_o is the initial surface roughness of undeformed coating, D_{max} (eq. (13)) is the average maximum grain size of undeformed coating; Y is the experimental constant, h_B is the thickness of the coating thin segment and h is the thickness of the coating thick segment at any given point. While the phase angle is denoted by θ and this varies between 0–π. The above equation considers surface roughness exhibiting periodicity of sine function and out of phase distribution for realistic modelling. Consequently, if $\theta = \pi/2$ then thickness h in eq. (14) reduces to $h = h_B + 2R_S$ which indicates in phase distribution of surface roughness.

3.3. Lubrication modelling

For fully separated lubricated contact (shown in Fig. 17) with Newtonian behaviour, the friction force directly depends on the mechanical, dimensional and rheological parameters (eq. (14)) [54]. For case with insufficient replenishment at the contact, the asperities can radically rise resulting in pressure increase and significant depletion of film thickness. In such situation, the lubricant starts behaving solid-like at boundary regime. Film thickness in relation to lubricant viscosity, sliding velocity and contact radius can be used to calculate friction force Q as [54],Where, a is the contact radius (refer to eq. (9)), u is the sliding velocity, η_o is the viscosity of bulk lubricant h_P is the thickness of uniform protection layer which is a key factor to reduce friction and wear and h_{oil} is the remaining thickness of the oil in vicinity of the asperity contact.

Now in relation to our wear analysis (section 3.1), the average coefficient of friction during fretting cycles i is defined as the ratio of friction and normal forces [55],

$$\overline{\mu} = \frac{1}{N}\sum_{i=1}^{N}\mu(i) \text{ where } \mu = \frac{Q}{P} \tag{15}$$

Substituting eq. (15) in eq. (14) yields,

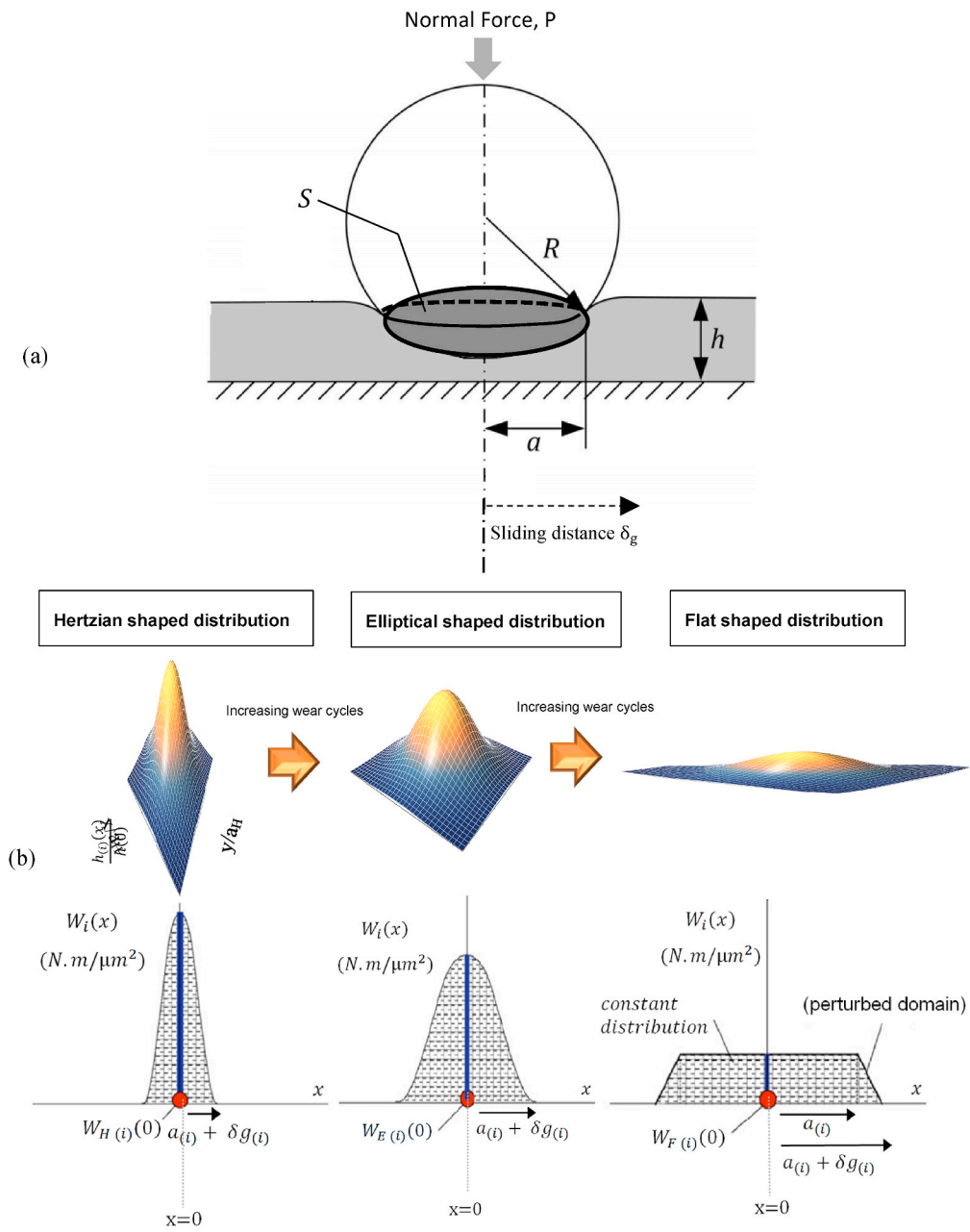$$\mu = \frac{\pi a^2 u \eta_o}{Ph_{oil\infty}} \tag{16}$$

Fig. 14. (a) shows the counter steel ball on coating with normal force (P), over-all sliding distance δ_g, contact radius a, radius of ball R, thickness of coating h and area of contact S while Fig. 14 (b) sketches the evolution of analysed Archard factor density $\sum W(0)$.
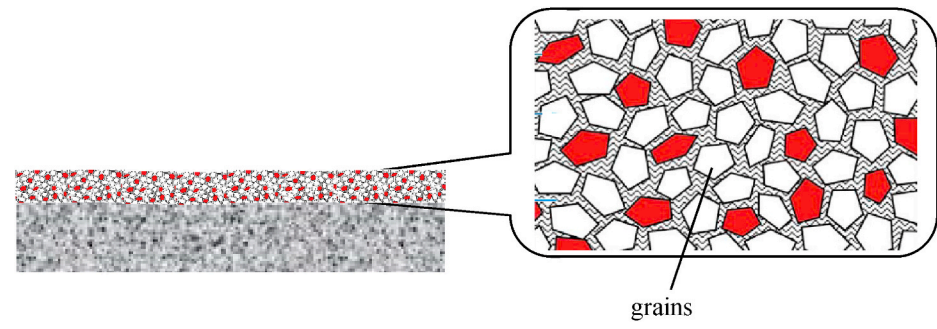

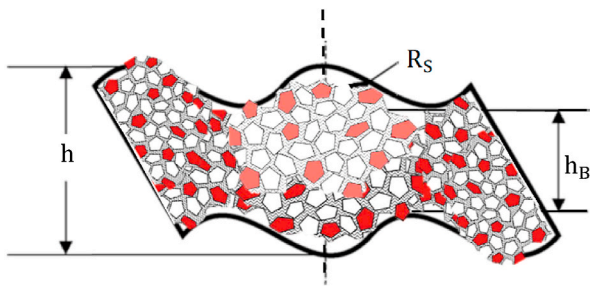**Fig. 15.** Schematic showing the grains of nanocomposite coating.

Fig. 16. Out of plane distribution surface roughness/asperities on nano-composite coating.

According to Cann [54] an essential assumption is that the thickness of film has a direct relation with the concentration of oil in the track. Another assumption was that the surface tension σ_s in the area around the contact decides the replenishment of the contact [54]. Therefore,

replenishment makes an inverse relation with the viscosity of oil, width of the track and sliding velocity. These parameters have been formulated in eq. (17), describing the changeover among the fully flooded regime and the starvation regime (starvation degree [SD]) [54].

$$SD = \frac{au\eta_o}{h_{oil\infty}\sigma_s} \tag{17}$$

Solving eqs. (17) and (16) gives coefficient of friction in terms of five parameters of SD as,

$$\mu = \frac{SD\sigma_s \, \pi a}{P} = \frac{u\eta_o \, \pi a^2}{P \, h_{oil\infty}} \tag{18}$$

Now to modify coefficient of friction in eq. (18) in terms of cumulated dissipated friction, eq. (7) and eq. (10) is substituted here in as,

$$\mu = \frac{u\eta_o\pi \left(\frac{4PR}{\pi L}\left(\frac{1-v_1^2}{E_1} + \frac{1-v_2^2}{E_2}\right)\right)^2}{P \, h_{oil\infty}} \tag{19}$$
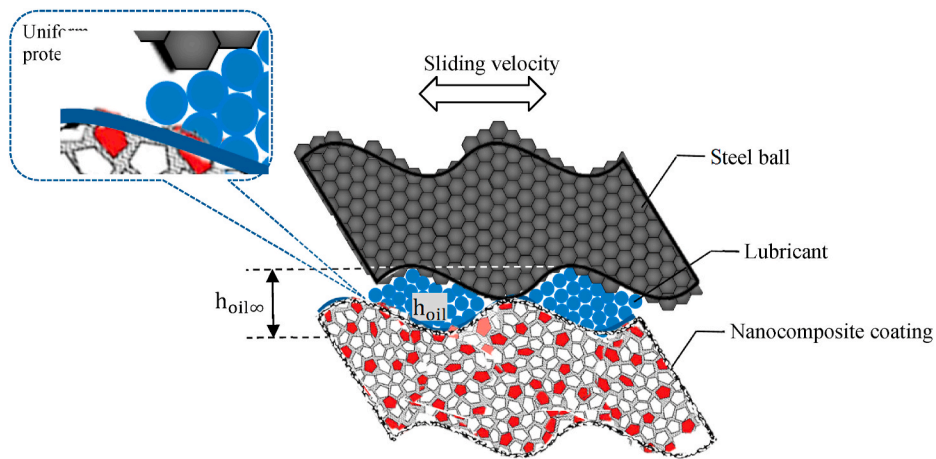

Fig. 17. Schematic shows the separated lubricated contact with between nanocomposite coating and counter carbon steel ball.

$$Q = \frac{\pi a^2 u\eta_o}{h_{oil\infty}} = \frac{\pi a^2 u\eta_o}{h_{oil\infty} \, h_p}; where \; h_{oil\infty} = h_{oil} + h_P \tag{14}$$
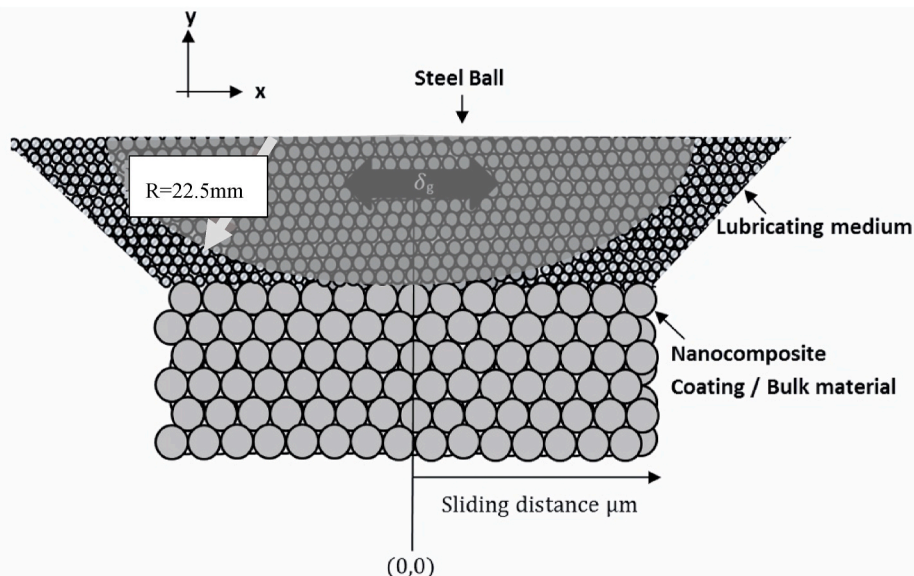

Fig. 18. The MD simulation model of nanocomposite coating sliding against counter carbon steel ball.

Table 4

The fitted material parameters which have been evaluated using MD simulation.

Materials	ν	E (GPa)	H (HV)	CTE (x 10^{-6}/K)	m	D_o (nm)
Ni/GPL	0.19 [57]	240 [38]	~480 [38]	13.3 [58]	1.5	11.21
Ni	0.3 [39]	190 [39]	266 [39]	13 [59]	1.3	23.08
Carbon Steel Ball	0.31 [60]	210 [60]	520 [60]	6.2 [61]		

Eq. (19) shows that friction coefficient is a complex attribute which in turn is a function of several wear, microstructural and lubrication parameters. It is noteworthy that in addition to nanocomposite coating properties, the friction coefficient is also in direct relation with the radius of steel ball R.

4. Modelling results and discussion

The validation of simulation results and the reliability of model was performed by comparing the results from MD simulations with the reported experimental results. LAAMP software [64,65] was used to simulate the fretting wear contact between Ni/GPL and counter carbon steel ball via 2nd order generation of reactive empirical bond order
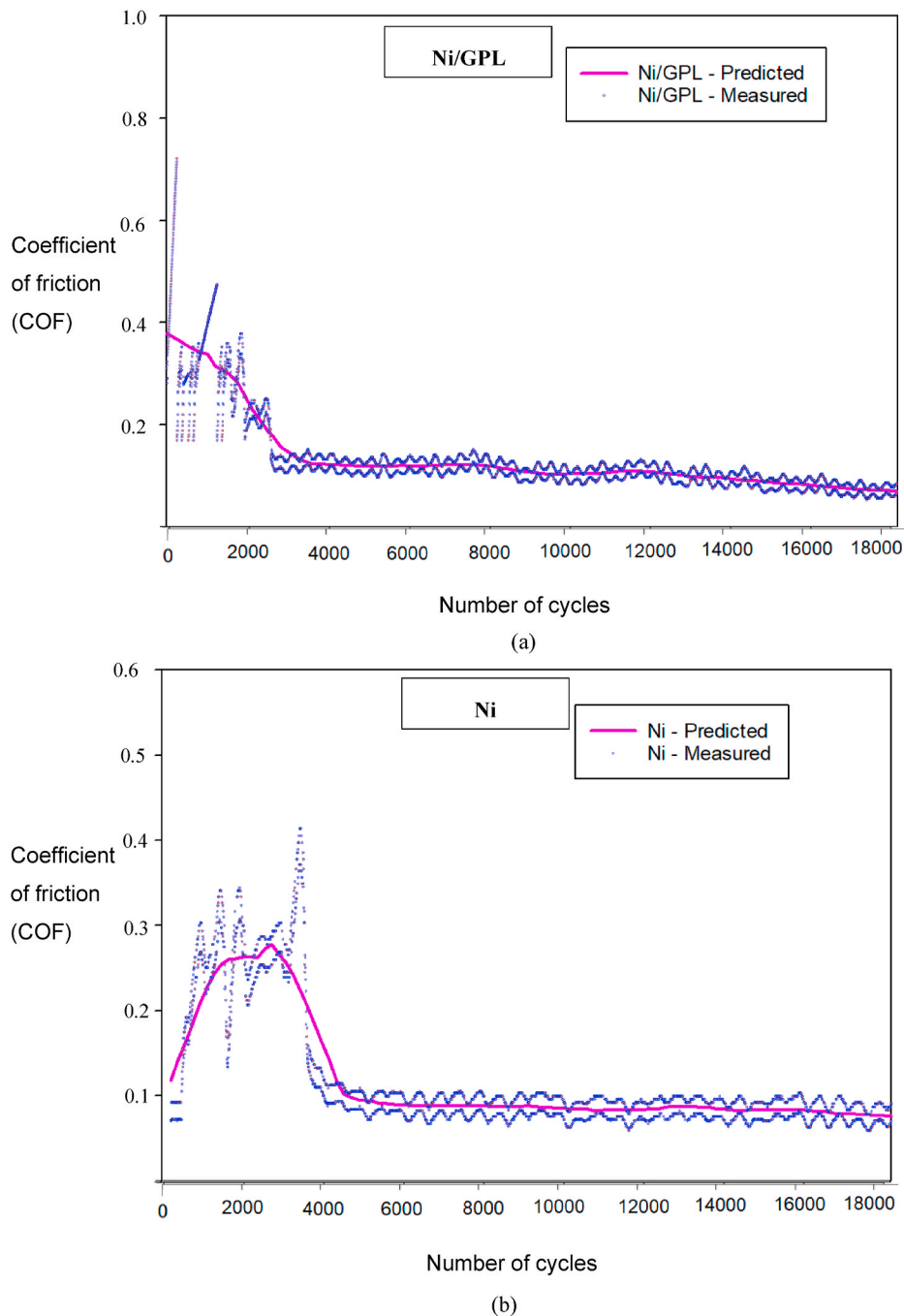

(a)

(b)

Fig. 19. Model validation using COF with respect to number of cycles for (a) Ni/GPL and (b) Ni at low oil viscosity η = 10 cST, φ = 28.64 mm, P0H = 2.00 GPa, Ra = 0.032 μm, δg = 100 μm.

(REBO) [19]. Embedded atom model was used to simulate the crystals potentials [66,67]. The simulation was conducted using Molecular statics framework with implementation using conjugate gradient method [67]. To maintain the constant level of system's energy, atoms and volume, the NVE boundary conditions were adopted [68]. The MD wear simulation model for Ni/GPL and Ni is illustrated in Fig. 18.

The simulation was based on nano-crystalline Ni-matrix and counter carbon steel ball with x and y axes taken as horizontal and vertical respectively to the coating surface according to the right-hand coordinate system. A well-defined arrangement along xy-plane consisting of 2.1×10^3 atoms with 95 atoms per layer along horizontal axis and a depth of total 25 layers along vertical axis was set to simulate the coating/ball interface. The outermost layer of Ni-matrix was originally indented at a specific depth by a semi-circular carbon steel ball. R = 22.5 mm was set as the original radius of ball. Both ball and Ni-matrix were enclosed by a lubricating medium. After some cycles, ball tip with sliding velocity of 0.1 m/s, began to wear out the Ni-matrix. The ball was assumed to be comparatively rigid to avoid the exchange of atoms amongst the Ni-matrix and the ball tip.

This work analysis the COF without plastic deformation. For Ni/GPL and Ni, the material parameter 'm' was obtained via MD simulations while additional material parameters were accessed from relevant research articles (see Table 4). These parameters were experimentally confirmed. The coating thickness was kept as 10 μm in accordance with the experiments, and all the coating parameters were strictly based on this thickness value.

To simulate the effects of various parameters including: wear, microstructural and lubrication on the COF (Fig. 19(a–b)) for both Ni/GPL and Ni, the values in Table 4 are used in the model. To validate the accuracy and reliability of model, COF for both Ni/GPL and Ni were compared with their corresponding experimental results. Both predicted and experimental results were in good agreement. The COF was plotted as a function of number of cycles. The predicted running-in period for Ni/GPL and Ni lasts for a few thousand cycles which is then followed by stable and steady state.

A slight divergence of predictive results from experimentally measured values was observed, which point towards the fact that the model somewhat over predicts some data points, however, this divergence was reduced by calibration of material parameter 'm'(shown in Table 4).

We will now focus our discussion on the influences of varying 'microstructural properties' for example thermal mismatch and percentage coating porosity of coating on the COF behaviour of Ni/GPL. For Ni/GPL, the predicted COF as a function of porosity percentage in relation to the number of stress cycles is shown in Fig. 20. At a given normal load of 2 GPa, the COF increased by 79% when coating percentage porosity increased from 2% to 6%. Porous surface account for large probability of generating wear debris due to large asperity-asperity contact. Consequently, the increase in COF with increasing porosity could be due to the creation of more asperity-asperity contact during sliding.

Fig. 21 demonstrates the influence of change in temperature ΔT from the initially fabricated temperature on the COF of Ni/GPL. The ΔT, because of the coating and substrate CTE mismatch, produces residual stress in coating [69]. The development of residual stress in coating due to CTE mismatch can also be observed during fretting cycles. Since CTE of Ni/GPL ($\alpha_c = 13.3 \times 10^{-6}$ K^{-1}) is larger than of steel substrate ($\alpha_s = 11.7 \times 10^{-6}$ K^{-1}) [70], the increase in temperature from fabrication temperature (ΔT = 50K) during wear testing results in the compressive residual stress in the coating while the decrease in temperature from fabrication temperature (ΔT = −50K) results in tensile residual stress in the coating [71]. The change in ΔT from −50K to 50K results in 61% rise in COF. The reason for higher COF for ΔT = 50K is that under compressive conditions the grain boundaries overlap [72] and constant compression under wear cycles consequences in surface deformation resulting in film breakdown causing relatively higher COF than ΔT = 0K and ΔT = −50K. Such higher COF is not observed when ΔT = −50K since constant tensile stress does not results in severe deformation thereby avoiding significantly high COF with wear cycles [73].

Further analysis was conducted by predicting the effect of counter carbon steel ball radii on COF. Typical variation of COF as a function of number of cycles at various ball radii is shown in Fig. 22. General trend was similar for various ball radii. From Fig. 22, it is observed that the COF in Ni/GPL increases with the ball radius due to increase in ball-coating contact area. In this case, the increase in contact area directly results in the increase of wear rate and corresponding COF. Furthermore, it can be seen that, the rise in COF as a result of increase in the ball radius from R = 22.5 mm–28.5 mm is not significantly large. This is
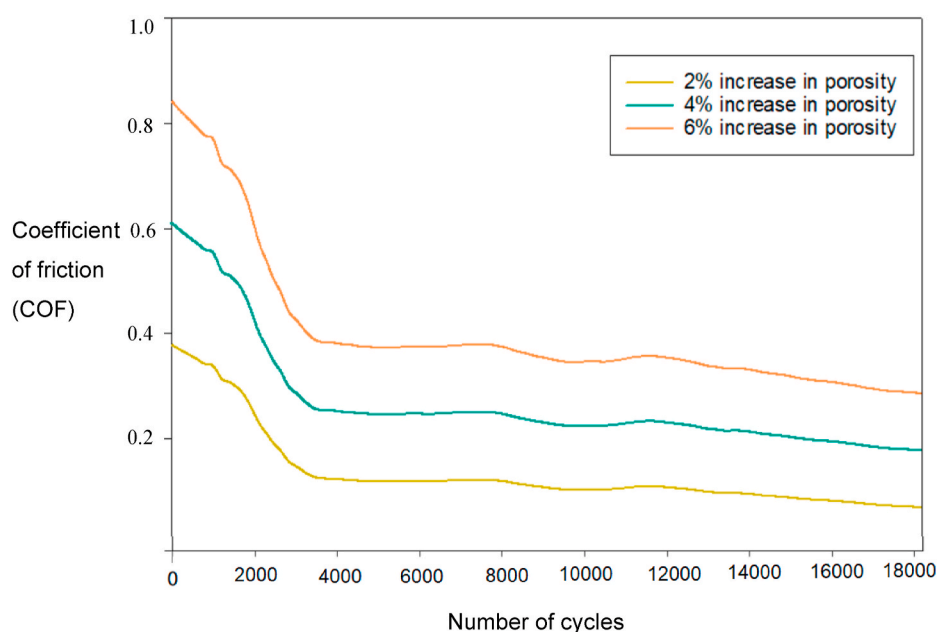

Fig. 20. The predicted COF for various percentage porosities of Ni/GPL at low oil viscosity η = 10 cST, φ = 28.64 mm, P0H = 2.00 GPa, Ra = 0.032 μm, δg = 100 μm.
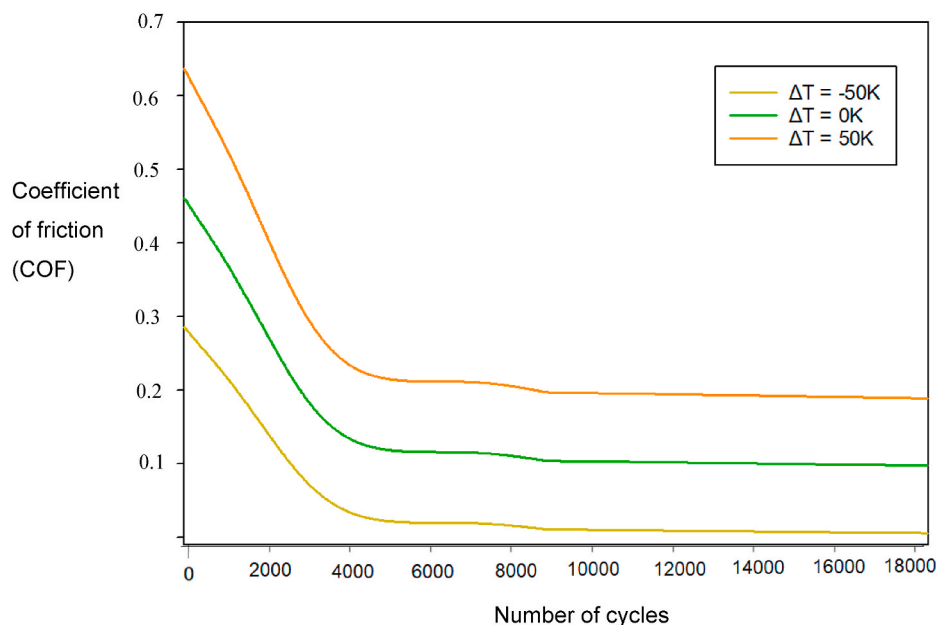
Fig. 21. The predicted COF for various CTE mismatch values of Ni/GPL at low oil viscosity η = 10 cST, φ = 28.64 mm, P0H = 2.00 GPa, Ra = 0.032 μm, δg = 100 μm.

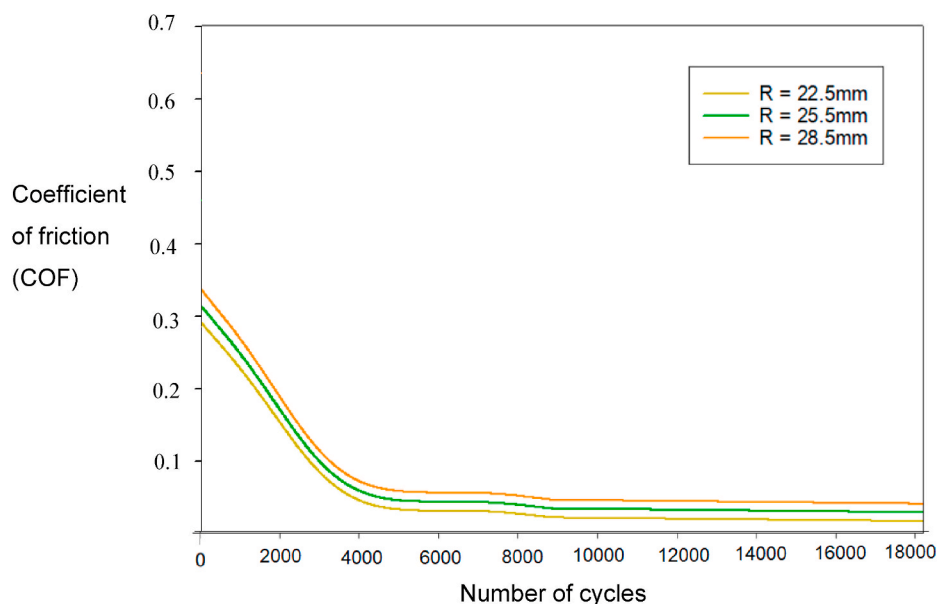**Fig. 22.** The predicted COF for various counter steel ball radii with respect to number of cycles for Ni/GPL at low oil viscosity η = 10 cST, φ = 28.64 mm, P0H = 2.00 GPa, Ra = 0.032 μm, δg = 100 μm.

possibly related to little micro-ploughing behaviour of Ni/GPL, producing less wear debris and in turn resulting in less rise in COF with varying ball sizes.

5. Conclusions

This work has presented frictional performance analysis of Nickel-Graphene (Ni/GPL) nanocomposite coating in comparison with pure Nickel (Ni) coating. The observations facilitated to develop a novel 2-D predictive numerical model to predict the coefficient of friction (COF) of Ni/GPL and Ni. The proposed new model is likewise valid for other types of nanocomposite coating. From the SEM results, the sliding wear response of both coatings in terms of hardness was also justified by the larger wear weight loss of counter carbon steel ball sliding against the

Ni/GPL compared to Ni. Further SEM analyses showed the narrow wear track in case of Ni/GPL compared to Ni. Moreover, the 3-D interferometric analysis of wear tracks revealed the "U-shaped" wear depth profiles of wear tracks which were utilised to calculate the energy distribution along the interface. A suite of 2-D predictive models has been developed on the basis of aforementioned experimental results integrating the wear, microstructural and lubrication equations to predict the COF of nanocomposite coatings. The COF predictions and the experimental results are in close agreement. The results explicitly showed the frictional performance of Ni/GPL nanocomposite coating in relation to increase in thermal mismatch, porosity, and counter ball radius. This work will result in significant savings in laborious, expensive experimental studies, as well as improved material life and reduction in unplanned breakdown costs.

CRediT authorship contribution statement

Mian Hammad Nazir: Conceptualization, Methodology, Software, Data curation, Writing – original draft. **Zulfiqar Ahmad Khan:** Data curation, Writing – original draft, Supervision. **Muhammad Majid Hussain:** Software, Validation. **Abdullah Rahil:** Visualization, Investigation. **Syed Zohaib Javaid Zaidi:** Writing – review & editing.

Declaration of competing interest

The authors declare the following financial interests/personal relationships which may be considered as potential competing interests: Mian Hammad Nazir reports a relationship with University of South Wales that includes: employment.

Data availability

The data that has been used is confidential.

References

[1] P.H.C. Camargo, K.G. Satyanarayana, F. Wypych, Nanocomposites: synthesis, structure, properties and new application opportunities, Mater. Res. 12 (1) (2009) 1–39.

[2] P. Jost, Economic Impact of Tribology, Proc mechanical failures prevention group, 1976, pp. 117–139.

[3] M.A. Meyers, A. Mishra, D.J. Benson, Mechanical properties of nanocrystalline materials, Prog. Mater. Sci. 51 (4) (2006) 427–556.

[4] K. Kumar, H. Van Swygenhoven, S. Suresh, Mechanical behavior of nanocrystalline metals and alloys, Acta Mater. 51 (19) (2003) 5743–5774.

[5] Y. Zong, L. Zuo, Materials design of microstructure in grain boundary and second phase particles, J. Mater. Sci. Technol. 19 (2) (2003) 97–101.

[6] W. Schwarzacher, Electrodeposition: a technology for the future, Electrochem. Soc. Interface 15 (1) (2006) 32–33.

[7] A. Möller, H. Hahn, Synthesis and characterization of nanocrystalline Ni/ZrO2 composite coatings, Nanostruct. Mater. 12 (1–4) (1999) 259–262.

[8] C. Low, R. Wills, F. Walsh, Electrodeposition of composite coatings containing nanoparticles in a metal deposit, Surf. Coating. Technol. 201 (1–2) (2006) 371–383.

[9] A. Karimpoor, U. Erb, K. Aust, G. Palumbo, High strength nanocrystalline cobalt with high tensile ductility, Scripta Mater. 49 (7) (2003) 651–656.

[10] P. Gyftou, M. Stroumbouli, E. Pavlatou, P. Asimidis, N. Spyrellis, Tribological study of Ni matrix composite coatings containing nano and micro SiC particles, Electrochim. Acta 50 (23) (2005) 4544–4550.

[11] H. Gül, F. Kılıç, S. Aslan, A. Alp, H. Akbulut, Characteristics of electro-co-deposited Ni–Al2O3 nano-particle reinforced metal matrix composite (MMC) coatings, Wear 267 (5–8) (2009) 976–990.

[12] R.S. Bajwa, Z. Khan, V. Bakolas, W. Braun, Water-lubricated Ni-based composite (Ni–Al 2 O 3, Ni–SiC and Ni–ZrO 2) thin film coatings for industrial applications, Acta Metall. Sin. 29 (1) (2016) 8–16.

[13] R.S. Bajwa, Z. Khan, V. Bakolas, W. Braun, Effect of bath ionic strength on adhesion and tribological properties of pure nickel and Ni-based nanocomposite coatings, J. Adhes. Sci. Technol. 30 (6) (2016) 653–665.

[14] J. Araújo, D. Nowell, Analysis of pad size effects in fretting fatigue using short crack arrest methodologies, Int. J. Fatig. 21 (9) (1999) 947–956.

[15] A. Begelinger, A. De Gee, Lubrication of sliding point contacts of AISI 52100 steel—the influence of curvature, Wear 36 (1) (1976) 7–11.

[16] X. Dai, K. Zhang, C. Tang, Friction and wear of pivot jewel bearing in oil-bath lubrication for high rotational speed application, Wear 302 (1–2) (2013) 1506–1513.

[17] I. McColl, J. Ding, S. Leen, Finite element simulation and experimental validation of fretting wear, Wear 256 (11–12) (2004) 1114–1127.

[18] L. Mattei, F. Di Puccio, B. Piccigallo, E. Ciulli, Lubrication and wear modelling of artificial hip joints: a review, Tribol. Int. 44 (5) (2011) 532–549.

[19] D.K. Karupannasamy, J. Hol, M.B. de Rooij, T. Meinders, D.J. Schipper, Modelling mixed lubrication for deep drawing processes, Wear 294–295 (2012) 296–304, https://doi.org/10.1016/j.wear.2012.06.006, 2012/07/30/.

[20] W. Qin, M. Wang, W. Sun, P. Shipway, X. Li, Modeling the effectiveness of oil lubrication in reducing both friction and wear in a fretting contact, Wear 426 (2019) 770–777.

[21] M.H. Nazir, Z.A. Khan, A. Saeed, V. Bakolas, W. Braun, R. Bajwa, Experimental analysis and modelling for reciprocating wear behaviour of nanocomposite coatings, Wear 416–417 (2018) 89–102, https://doi.org/10.1016/j.wear.2018.09.011, 2018/12/15/.

[22] M.H. Nazir, Z.A. Khan, A. Saeed, K. Stokes, Modeling the effect of residual and diffusion-induced stresses on corrosion at the interface of coating and substrate, Corrosion 72 (4) (2016/04/01 2015) 500–517, https://doi.org/10.5006/1804.

[23] M.H. Nazir, Z.A. Khan, A. Saeed, K. Stokes, A predictive model for life assessment of automotive exhaust mufflers subject to internal corrosion failure due to exhaust

gas condensation, Eng. Fail. Anal. 63 (2016) 43–60, https://doi.org/10.1016/j.engfailanal.2016.02.014.

[24] M.H. Nazir, Z.A. Khan, K. Stokes, A holistic mathematical modelling and simulation for cathodic delamination mechanism – a novel and an efficient approach, J. Adhes. Sci. Technol. (2015) 1–39, https://doi.org/10.1080/01694243.2015.1071023.

[25] M.H. Nazir, Z. Khan, K. Stokes, Modelling of metal-coating delamination incorporating variable environmental parameters, J. Adhes. Sci. Technol. 29 (5) (2014) 392–423.

[26] M. Nazir, Z. Khan, A. Saeed, K. Stokes, Modelling the Effect of Residual and Diffusion Induced Stresses on Corrosion at the Interface of Coating and Substrate, Corrosion, 2015.

[27] M.H. Nazir, Z.A. Khan, K. Stokes, Optimisation of interface roughness and coating thickness to maximise coating-substrate adhesion - a failure prediction and reliability assessment modelling, J. Adhes. Sci. Technol. 29 (14) (2015) 1415–1445, https://doi.org/10.1080/01694243.2015.1026870.

[28] A. Saeed, Z.A. Khan, M.H. Nazir, Time dependent surface corrosion analysis and modelling of automotive steel under a simplistic model of variations in environmental parameters, Mater. Chem. Phys. 178 (2016) 65–73, https://doi.org/10.1016/j.matchemphys.2016.04.068, 8/1/.

[29] M. Nazir, Z.A. Khan, K. Stokes, A unified mathematical modelling and simulation for cathodic blistering mechanism incorporating diffusion and fracture mechanics concepts, J. Adhes. Sci. Technol. 29 (12) (2015) 1200–1228.

[30] M.H. Nazir, Z.A. Khan, K. Stokes, Analysing the coupled effects of compressive and diffusion induced stresses on the nucleation and propagation of circular coating blisters in the presence of micro-cracks, Eng. Fail. Anal. 70 (2016) 1–15, https://doi.org/10.1016/j.engfailanal.2016.07.003.

[31] M.H. Nazir, A. Saeed, Z. Khan, A comprehensive predictive corrosion model incorporating varying environmental gas pollutants applied to wider steel applications, Mater. Chem. Phys. 193 (2017) 19–34.

[32] M. Nazir, Z. Khan, A Review of Theoretical Analysis Techniques for Cracking and Corrosive Degradation of Film-Substrate Systems, Engineering Failure Analysis, 2016.

[33] R. Bajwa, Z. Khan, H. Nazir, V. Chacko, A. Saeed, Wear and friction properties of electrodeposited Ni-based coatings subject to nano-enhanced lubricant and composite coating, Acta Metall. Sin. 29 (10) (2016) 902–910.

[34] M.H. Nazir, Z. Khan, Maximising the interfacial toughness of thin coatings and substrate through optimisation of defined parameters, Int. J. Comput. Method. Experiment. Measure. 3 (4) (2015) 316–328.

[35] R.S. Bajwa, Z. Khan, V. Bakolas, W. Braun, Water-lubricated Ni-based composite (Ni–Al2O3, Ni–SiC and Ni–ZrO2) thin film coatings for industrial applications, Acta Metall. Sin. 29 (1) (2015) 8–16.

[36] M.H. Nazir, et al., Analyzing and modelling the corrosion behavior of Ni/Al2O3, Ni/SiC, Ni/ZrO2 and Ni/Graphene nanocomposite coatings, Materials 10 (11) (2017) 1225.

[37] M. Prince, A.J. Thanu, P. Gopalakrishnan, Improvement in wear and corrosion resistance of AISI 1020 steel by high velocity oxy-fuel spray coating containing Ni-Cr-B-Si-Fe-C, High Temp. Mater. Process. 31 (2012) 149.

[38] A. Li, I. Szlufarska, How grain size controls friction and wear in nanocrystalline metals, Phys. Rev. B 92 (7) (2015), 075418.

[39] B. Zabala, et al., Friction and wear of a piston ring/cylinder liner at the top dead centre: experimental study and modelling, Tribol. Int. 106 (2017) 23–33.

[40] H. Cao, Z. Khan, Y. Meng, Comparison of rolling contact fatigue life between elastohydrodynamic lubricated point contacts pre and post running-in treatment, Tribol. Int. 144 (2020), 106089, https://doi.org/10.1016/j.triboint.2019.106089, 2020/04/01/.

[41] C. Ma, S. Wang, L. Wang, F. Walsh, R. Wood, The role of a tribofilm and wear debris in the tribological behaviour of nanocrystalline Ni–Co electrodeposits, Wear 306 (1–2) (2013) 296–303.

[42] L. Bai, Y. Meng, Z.A. Khan, V. Zhang, The synergetic effects of surface texturing and MoDDP additive applied to ball-on-disk friction subject to both flooded and starved lubrication conditions, Tribol. Lett. 65 (4) (2017) 163, https://doi.org/10.1007/s11249-017-0949-y, 2017/11/07.

[43] P.J. Blau, On the nature of running-in, Tribol. Int. 38 (11–12) (2005) 1007–1012.

[44] D. Berman, A. Erdemir, A.V. Sumant, Few layer graphene to reduce wear and friction on sliding steel surfaces, Carbon 54 (2013) 454–459.

[45] D. Berman, A. Erdemir, A.V. Sumant, Reduced wear and friction enabled by graphene layers on sliding steel surfaces in dry nitrogen, Carbon 59 (2013) 167–175.

[46] "3 - fundamentals of contact mechanics and friction, in: G. Chen (Ed.), Handbook of Friction-Vibration Interactions, Woodhead Publishing, 2014, pp. 71–152.

[47] M. Cloitre, R.T. Bonnecaze, A review on wall slip in high solid dispersions, Rheol. Acta 56 (3) (2017) 283–305, https://doi.org/10.1007/s00397-017-1002-7, 2017/03/01.

[48] A. Jabbar, et al., Electrochemical deposition of nickel graphene composite coatings: effect of deposition temperature on its surface morphology and corrosion resistance, RSC Adv. 7 (49) (2017) 31100–31109.

[49] Z. Ren, et al., Mechanical properties of nickel-graphene composites synthesized by electrochemical deposition, Nanotechnology 26 (6) (2015), 065706.

[50] P.D. Harvey, Engineering Properties of Steel, Asm Intl, 1982.

[51] B. Selcuk, R. Ipek, M. Karamış, A study on friction and wear behaviour of carburized, carbonitrided and borided AISI 1020 and 5115 steels, J. Mater. Process. Technol. 141 (2) (2003) 189–196.

[52] M. Kalin, J. Vižintin, S. Novak, G. Dražič, Wear mechanisms in oil-lubricated and dry fretting of silicon nitride against bearing steel contacts, Wear 210 (1–2) (1997) 27–38.

[53] H. Al-Qureshi, A. Klein, M. Fredel, Grain size and surface roughness effect on the instability strains in sheet metal stretching, J. Mater. Process. Technol. 170 (1–2) (2005) 204–210.

[54] P. Cann, B. Damiens, A. Lubrecht, The transition between fully flooded and starved regimes in EHL, Tribol. Int. 37 (10) (2004) 859–864.

[55] S. Fouvry, T. Liskiewicz, C. Paulin, A global–local wear approach to quantify the contact endurance under reciprocating-fretting sliding conditions, Wear 263 (1) (2007) 518–531.

[56] M.H. Nazir, Z.A. Khan, A. Saeed, A. Siddaiah, P.L. Menezes, Synergistic wear-corrosion analysis and modelling of nanocomposite coatings, Tribol. Int. 121 (2018) 30–44, https://doi.org/10.1016/j.triboint.2018.01.027, 2018/05/01/.

[57] S. Fouvry, T. Liskiewicz, C. Paulin, A global–local wear approach to quantify the contact endurance under reciprocating-fretting sliding conditions, Wear 263 (1–6) (2007) 518–531.

[58] H. Proudhon, S. Fouvry, J.Y. Buffière, A fretting crack initiation prediction taking into account the surface roughness and the crack nucleation process volume, Int. J. Fatig. 27 (5) (2005) 569–579, https://doi.org/10.1016/j.ijfatigue.2004.09.001, 2005/05/01/.

[59] P.A. Witherspoon, J.S. Wang, K. Iwai, J.E. Gale, Validity of cubic law for fluid flow in a deformable rock fracture, Water Resour. Res. 16 (6) (1980) 1016–1024.

[60] Q. Lei, W. Xiong, J. Yuang, Y. Cui, Y.-S. Wu, Analysis of stress sensitivity and its influence on oil production from tight reservoirs, in: Eastern Regional Meeting, Society of Petroleum Engineers, 2007.

[61] F.-Z. Xuan, L.-Q. Cao, Z. Wang, S.-T. Tu, Mass transport in laser surface nitriding involving the effect of high temperature gradient: simulation and experiment, Comput. Mater. Sci. 49 (1) (2010) 104–111.

[62] S. Whitaker, Flow in porous media I: a theoretical derivation of Darcy's law, Transport Porous Media 1 (1) (1986) 3–25.

[63] C.-H. Hsueh, Modeling of elastic deformation of multilayers due to residual stresses and external bending, J. Appl. Phys. 91 (12) (2002) 9652–9656.

[64] http://lammps.sandia.gov ".

[65] S. Plimpton, Fast parallel algorithms for short-range molecular dynamics, J. Comput. Phys. 117 (1) (1995) 1–19.

[66] S. Foiles, M. Baskes, M. Daw, Embedded-atom-method functions for the fcc metals Cu, Ag, Au, Ni, Pd, Pt, and their alloys, Phys. Rev. B 33 (12) (1986) 7983.

[67] M. Mendelev, S. Han, D. Srolovitz, G. Ackland, D. Sun, M. Asta, Development of new interatomic potentials appropriate for crystalline and liquid iron, Phil. Mag. 83 (35) (2003) 3977–3994.

[68] S. Goel, N.H. Faisal, V. Ratia, A. Agrawal, A. Stukowski, Atomistic investigation on the structure–property relationship during thermal spray nanoparticle impact, Comput. Mater. Sci. 84 (2014) 163–174.

[69] M. Nazir, Z.A. Khan, K. Stokes, Optimisation of interface roughness and coating thickness to maximise coating–substrate adhesion–a failure prediction and reliability assessment modelling, J. Adhes. Sci. Technol. 29 (14) (2015) 1415–1445.

[70] D.R. Lide, CRC Handbook of Chemistry and Physics, 1947, p. 12J204.

[71] M. Nazir, Z.A. Khan, A. Saeed, K. Stokes, Modeling the effect of residual and diffusion-induced stresses on corrosion at the interface of coating and substrate, Corrosion 72 (4) (2015) 500–517.

[72] E. TobyáKelsey, N.H. áde Leeuw, Atomistic simulation of dislocations, surfaces and interfaces in MgO, J. Chem. Soc., Faraday Trans. 92 (3) (1996) 433–438.

[73] W.T. Read, W. Shockley, Dislocation models of crystal grain boundaries, Phys. Rev. 78 (3) (1950) 275.